



A Self-Supervised Deep Learning Reconstruction for Shortening the Breathhold and Acquisition Window in Cardiac Magnetic Resonance Fingerprinting

Jesse I. Hamilton^{1,2*}

¹ Department of Radiology, University of Michigan, Ann Arbor, MI, United States, ² Department of Biomedical Engineering, University of Michigan, Ann Arbor, MI, United States

OPEN ACCESS

Edited by:

Anthony G. Christodoulou,
Cedars Sinai Medical Center,
United States

Reviewed by:

Ruixi Zhou,
Beijing University of Posts
and Telecommunications (BUPT),
China
Haikun Qi,
ShanghaiTech University, China

*Correspondence:

Jesse I. Hamilton
hamiljes@med.umich.edu

Specialty section:

This article was submitted to
Cardiovascular Imaging,
a section of the journal
Frontiers in Cardiovascular Medicine

Received: 25 April 2022

Accepted: 06 June 2022

Published: 23 June 2022

Citation:

Hamilton JI (2022) A
Self-Supervised Deep Learning
Reconstruction for Shortening
the Breathhold and Acquisition
Window in Cardiac Magnetic
Resonance Fingerprinting.
Front. Cardiovasc. Med. 9:928546.
doi: 10.3389/fcvm.2022.928546

The aim of this study is to shorten the breathhold and diastolic acquisition window in cardiac magnetic resonance fingerprinting (MRF) for simultaneous T_1 , T_2 , and proton spin density (M_0) mapping to improve scan efficiency and reduce motion artifacts. To this end, a novel reconstruction was developed that combines low-rank subspace modeling with a deep image prior, termed DIP-MRF. A system of neural networks is used to generate spatial basis images and quantitative tissue property maps, with training performed using only the undersampled k-space measurements from the current scan. This approach avoids difficulties with obtaining *in vivo* MRF training data, as training is performed *de novo* for each acquisition. Calculation of the forward model during training is accelerated by using GRAPPA operator gridding to shift spiral k-space data to Cartesian grid points, and by using a neural network to rapidly generate fingerprints in place of a Bloch equation simulation. DIP-MRF was evaluated in simulations and at 1.5 T in a standardized phantom, 18 healthy subjects, and 10 patients with suspected cardiomyopathy. In addition to conventional mapping, two cardiac MRF sequences were acquired, one with a 15-heartbeat(HB) breathhold and 254 ms acquisition window, and one with a 5HB breathhold and 150 ms acquisition window. In simulations, DIP-MRF yielded decreased nRMSE compared to dictionary matching and a sparse and locally low rank (SLLR-MRF) reconstruction. Strong correlation ($R^2 > 0.999$) with T_1 and T_2 reference values was observed in the phantom using the 5HB/150 ms scan with DIP-MRF. DIP-MRF provided better suppression of noise and aliasing artifacts *in vivo*, especially for the 5HB/150 ms scan, and lower intersubject and intrasubject variability compared to dictionary matching and SLLR-MRF. Furthermore, it yielded a better agreement between myocardial T_1 and T_2 from 15HB/254 ms and 5HB/150 ms MRF scans, with a bias of -9 ms for T_1 and 2 ms for T_2 . In summary, this study introduces an extension of the deep image prior framework for cardiac MRF tissue property mapping, which does not require pre-training with *in vivo* scans, and has the potential to reduce motion artifacts by enabling a shortened breathhold and acquisition window.

Keywords: deep learning, deep image prior, cardiovascular imaging, low rank, multiparametric magnetic resonance imaging (MRI), magnetic resonance fingerprinting (MRF), T_1 mapping, T_2 mapping

INTRODUCTION

Cardiac magnetic resonance (CMR) T_1 and T_2 mapping are useful for the detection of pathological changes in myocardial tissue, including acute (1) and chronic inflammation (2, 3), edema (4, 5), amyloid deposition (6), fatty infiltration (7), and infarct (8). Multiparametric methods have recently been developed to efficiently measure multiple tissue properties during one scan (9–12). Cardiac magnetic resonance fingerprinting (MRF) is one such technique that uses a time-varying pulse sequence to encode several properties in magnetization signal evolutions over time (13, 14). A time series of highly undersampled images is acquired, typically with a single image frame collected per repetition time (TR). Quantitative maps are obtained using pattern recognition, where the signal evolution (or “fingerprint”) measured at each voxel is matched to a dictionary of fingerprints simulated for different tissue property values.

While simultaneous T_1 , T_2 , and proton spin density (M_0) mapping using cardiac MRF has been demonstrated in healthy subjects (15) and cardiomyopathy patients (16), respiratory and cardiac motion present significant challenges, even when breathholding and electrocardiogram (ECG) triggering are employed. The highly accelerated non-Cartesian sampling used in cardiac MRF introduces noise-like artifacts in the measured fingerprints, and thus many image frames are collected to enable accurate pattern recognition using the corrupted signals. Several previous studies employed a relatively long breathhold of 15 heartbeats and diastolic acquisition window of approximately 250 ms as a result (15). However, this sequence may be susceptible to motion if patients have difficulty holding their breath or have elevated heart rates. While retrospective motion correction can be used (17), an alternative strategy is to shorten the breathhold and acquisition window to avoid the need for such corrections.

Shortening the MRF acquisition will result in fewer time points in each fingerprint, which can impede accurate pattern recognition. Several classes of reconstruction methods have been developed to accelerate MRF scans, including model-based reconstructions (18, 19), low-rank subspace techniques (20–22), and deep learning (23). Deep learning methods have gained particular interest for their excellent denoising capabilities and fast computation times. While some MRF deep learning reconstructions operate on single-voxel fingerprints (23, 24), others use the fingerprints from many voxels within a spatial neighborhood to estimate the tissue properties at a target voxel (25), and thus can leverage both spatial and temporal correlations in the MRF data to reduce noise and k-space undersampling artifacts. Such a method was recently demonstrated for MRF in the brain, where a convolutional neural network (CNN) reconstruction enabled a 4-fold reduction in scan time compared to conventional dictionary matching (25) and allowed for high-resolution (submillimeter) mapping (26).

However, CNN reconstructions typically require training using *in vivo* datasets, which presents a challenge for cardiac MRF. It is difficult to collect ground truth tissue property maps in the heart due to physiological motion, as a scan time of several minutes would be needed to obtain fully-sampled MRF data.

Furthermore, because the MRF scan is prospectively triggered, the fingerprints depend on the subject’s cardiac rhythm (14), and thus many datasets from subjects with different cardiac rhythms (including fast or irregular rhythms commonly seen in patients) would potentially be needed for training.

Recently, a deep image prior (DIP) technique was proposed for image processing tasks that does not require pre-training with ground truth datasets (27). Taking image denoising as an example, a randomly initialized CNN learns to generate a denoised image by minimizing the mean squared error loss compared to a noise-corrupted image, with no requirements for additional training data. The network architecture is typically based on a u-net (28) and is designed so that lower spatial frequencies are recovered before higher spatial frequencies (29). Therefore, the network learns to generate natural images before recovering higher frequency noise, so that training with early stopping avoids overfitting to the noisy image. When applied to inverse problems in medical imaging, a mathematical model of the image acquisition can be incorporated in the loss function, which has been applied to computed tomography (30), positron emission tomography (31), and diffusion MRI (32).

This study introduces a self-supervised deep learning reconstruction for cardiac MRF T_1 , T_2 , and M_0 mapping for the purpose of mitigating noise, reducing k-space undersampling artifacts, and enabling a shortened acquisition to reduce motion artifacts. The proposed method, termed DIP-MRF, combines low-rank MRF subspace modeling with the denoising capabilities of a deep image prior. A system of convolutional (u-net) and fully-connected networks is used to generate spatial basis images (i.e., images in a low-dimensional subspace derived from the MRF signal evolutions) and quantitative maps, without dictionary matching and without pre-training using *in vivo* data. For each MRF acquisition, training is performed *de novo* using only the undersampled k-space measurements from the current scan by incorporating a mathematical model of the cardiac MRF data acquisition in the loss function. DIP-MRF is shown to reduce noise and undersampling artifacts compared to conventional dictionary matching and low-rank subspace reconstructions. Furthermore, DIP-MRF is leveraged to shorten the breathhold duration from 15 to 5 heartbeats and diastolic acquisition window from 250 to 150 ms, with results shown in healthy subjects and cardiomyopathy patients, which has the potential to reduce motion artifacts.

MATERIALS AND METHODS

Previous work has shown that an MRF dictionary, denoted by $D \in \mathbb{C}^p \times t$, where p is the number of parameter combinations and t is the number of time points, can be compressed along time using a truncated singular value decomposition (SVD) that retains only the first k singular values (33). The temporal basis functions are denoted by $V_k \in \mathbb{C}^t \times k$, which is matrix whose columns contain the first k right singular vectors. A compressed dictionary, denoted by $D_k \in \mathbb{C}^p \times k$, can be obtained according to $D_k = DV_k$. Similarly, if $x \in \mathbb{C}^n \times t$ denotes a time series of MRF images with n voxels, then multiplication by V_k yields

a set of spatial basis images in this low-dimensional subspace, denoted by $x_k = xV_k$, where $x_k \in \mathbb{C}^{n \times k}$. Multiplying the spatial basis images by the complex conjugate V_k^* will yield a low-rank approximation to the original MRF image series, $x \approx x_k V_k^*$. Low-rank subspace reconstructions for MRF have been proposed that iteratively remove noise and undersampling artifacts from the spatial basis images, sometimes with additional regularization terms using spatial sparsity and/or locally low rank regularization, before matching to the compressed dictionary to obtain quantitative maps (21, 22, 34, 35).

This study extends the deep image prior framework using a low-rank cardiac MRF signal model. An overview of the DIP-MRF reconstruction pipeline is shown in **Figure 1**. A convolutional u-net generates spatial basis images, which are input to a fully-connected network that outputs quantitative maps, neither of which require pre-training with *in vivo* data. Rather, the networks are trained in a self-supervised manner to enforce consistency with the undersampled k-space data from a single scan by incorporating the MRF forward encoding model in the loss function. The forward model includes (1) simulation of a time series of MRF images from the tissue property maps, (2) projection of images onto the low-dimensional subspace, (3) coil sensitivity encoding, and (4) spiral k-space undersampling. Calculation of the forward model is accelerated by (1) a pre-trained neural network that rapidly outputs fingerprints instead of using a more time-consuming Bloch equation simulation (36), and (2) preprocessing the spiral MRF k-space data with GRAPPA operator gridding (GROG) to obtain data in Cartesian k-space (37). The following sections will describe the DIP-MRF pipeline in more detail.

Pre-trained Fingerprint Generator Network

Calculating the forward model requires repeated simulations of MRF signal evolutions at every iteration. To reduce computation time, this step is performed using a neural network called the Fingerprint Generator Network (FGN), which rapidly outputs signal evolutions for arbitrary T_1 , T_2 , and cardiac rhythm timings (**Figure 2A**) and has been described previously (36). The network is fully-connected with two hidden layers and 300 nodes per layer. The input consists of a T_1 value, a T_2 value, and the subject's cardiac rhythm timings (specifically, a vector of RR interval times) recorded by the ECG during the scan. The output is a vector of length $2t$ containing interleaved real and imaginary parts of the fingerprint. The FGN is the only neural network component in the DIP-MRF pipeline that requires pre-training. The pre-training is performed only one time using fingerprints produced by a Bloch equation simulation for different T_1 , T_2 , and cardiac rhythm timings, after which the same network can be applied to any subsequent scan regardless of the subject's cardiac rhythm. **Supplementary Figure 1** gives additional details about pre-training the FGN.

Low-Rank Signal Approximation

Although DIP-MRF does not use pattern recognition, a dictionary of fingerprints is calculated temporarily in order to

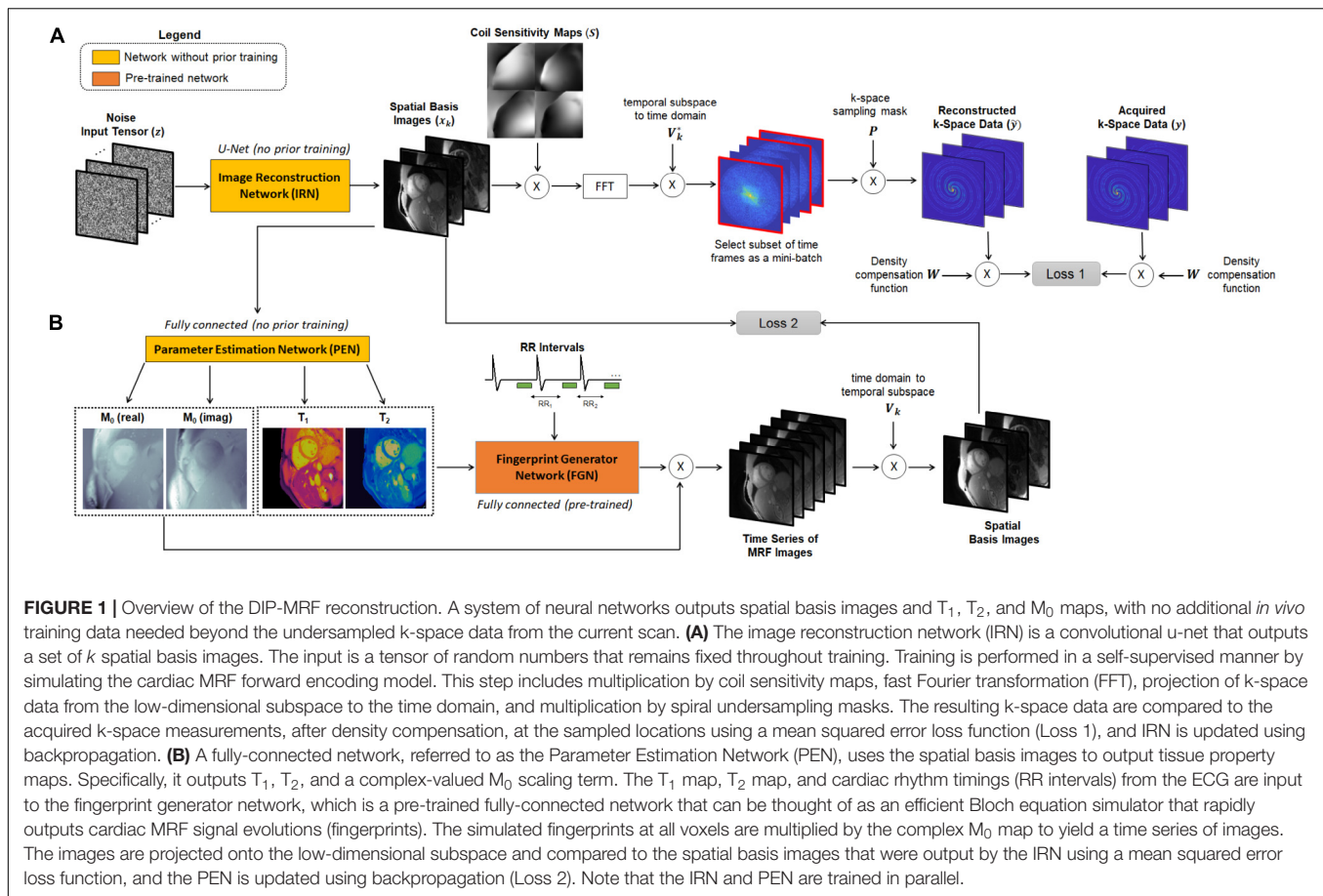
derive the temporal basis functions V_k (33). The FGN is used to output a dictionary of approximately 23,000 fingerprints with T_1 between 50–3,000 ms and T_2 between 5–1,000 ms, which takes 30 ms on a GPU. Next, the SVD of the dictionary is calculated (taking approximately 1 s), and the temporal basis functions are obtained from the first k right singular vectors (**Figure 2B**). This study uses a rank of $k = 5$, which retains more than 99.9% of the energy compared to the uncompressed fingerprints.

GRAPPA Operator Gridding Preprocessing and Coil Sensitivity Estimation

The forward model calculation requires repeated iterations between image and k-space domains. To avoid time-consuming operations using the non-uniform fast Fourier Transform (NUFFT) (38), the MRF spiral k-space data are preprocessed using GROG, a parallel imaging technique that shifts non-Cartesian k-space data to unmeasured Cartesian locations using GRAPPA weight matrices (37). The weight matrices for unit shifts along k_x and k_y are calibrated using a fully-sampled dataset; this dataset is obtained by taking the temporal average of the multicoil MRF k-space data, gridding a time-averaged image using the NUFFT, and performing an FFT to obtain multicoil Cartesian k-space data. The central 48×48 region of the Cartesian k-space is used for GROG calibration. Coil sensitivity maps are estimated from the time-averaged multicoil images using the adaptive combination method (39). The GROG density compensation function, denoted by W , is obtained by counting the number of spiral k-space points that are shifted to each Cartesian coordinate. After calibration, the GROG weights are applied to shift undersampled spiral MRF k-space data onto a Cartesian grid, and each time frame of the resulting Cartesian k-space dataset is multiplied by W . A binary mask, denoted by P_i , is stored that indicates the sampled (acquired) points on the Cartesian grid at each time index i .

Neural Network Architectures

A convolutional u-net, which is not pre-trained, is used to output the MRF spatial basis images. This network will be called the image reconstruction network (IRN) and is shown in **Figure 3**. Inspired by the original DIP publication (27), the input is a tensor denoted by $z \in \mathbb{R}^{n_y \times n_x \times d}$ of uniform random numbers between -0.1 and 0.1 , where n_y and n_x are the spatial dimensions in voxels, and d is a tunable parameter defining the number of feature channels in the first layer of the network. This study uses $d = 32$ to be consistent with the original DIP work, but this parameter was not found to have much impact on the reconstruction. The IRN performs a series of 2D convolutions followed by batch normalization, leaky ReLU activation, and an optional dropout layer. The data pass through five downsampling and upsampling paths with multiple skip connections. Downsampling is implemented using convolution with a 2×2 stride, and upsampling is performed using nearest neighbor interpolation followed by convolution. The network output has size $n_y \times n_x \times 2k$, where the channel



dimension contains the interleaved real and imaginary parts of the k spatial basis images.

A fully-connected network, which also is not pre-trained, outputs quantitative T_1 , T_2 , and M_0 maps from the spatial basis images. This network will be called the parameter estimation network (PEN) and is shown in **Figure 4**. The PEN has two hidden layers with 300 nodes per layer. Before being input to the network, the spatial basis images are vectorized to have size $(n_y n_x) \times (2k)$, where the second (channel) dimension contains interleaved real and imaginary signal intensities. The network output has one channel for each tissue property. As in previous MRF studies (13, 14), M_0 is modeled as a complex-valued scaling factor between the measured and simulated fingerprints, so the output has four channels for T_1 , T_2 , and the real and imaginary parts of M_0 .

Self-Supervised Training

The IRN and PEN networks are trained *de novo* for each reconstruction in a self-supervised manner (**Figure 1**). Both networks are initialized with random weights and biases. Additionally, the input (z) to the IRN is initialized with random numbers and remains fixed throughout training. Both networks are trained in parallel using a loss function with two terms, one for updating each network. First, letting θ_{IRN} denote the network

parameters of the IRN, the spatial basis images generated by the IRN can be written as,

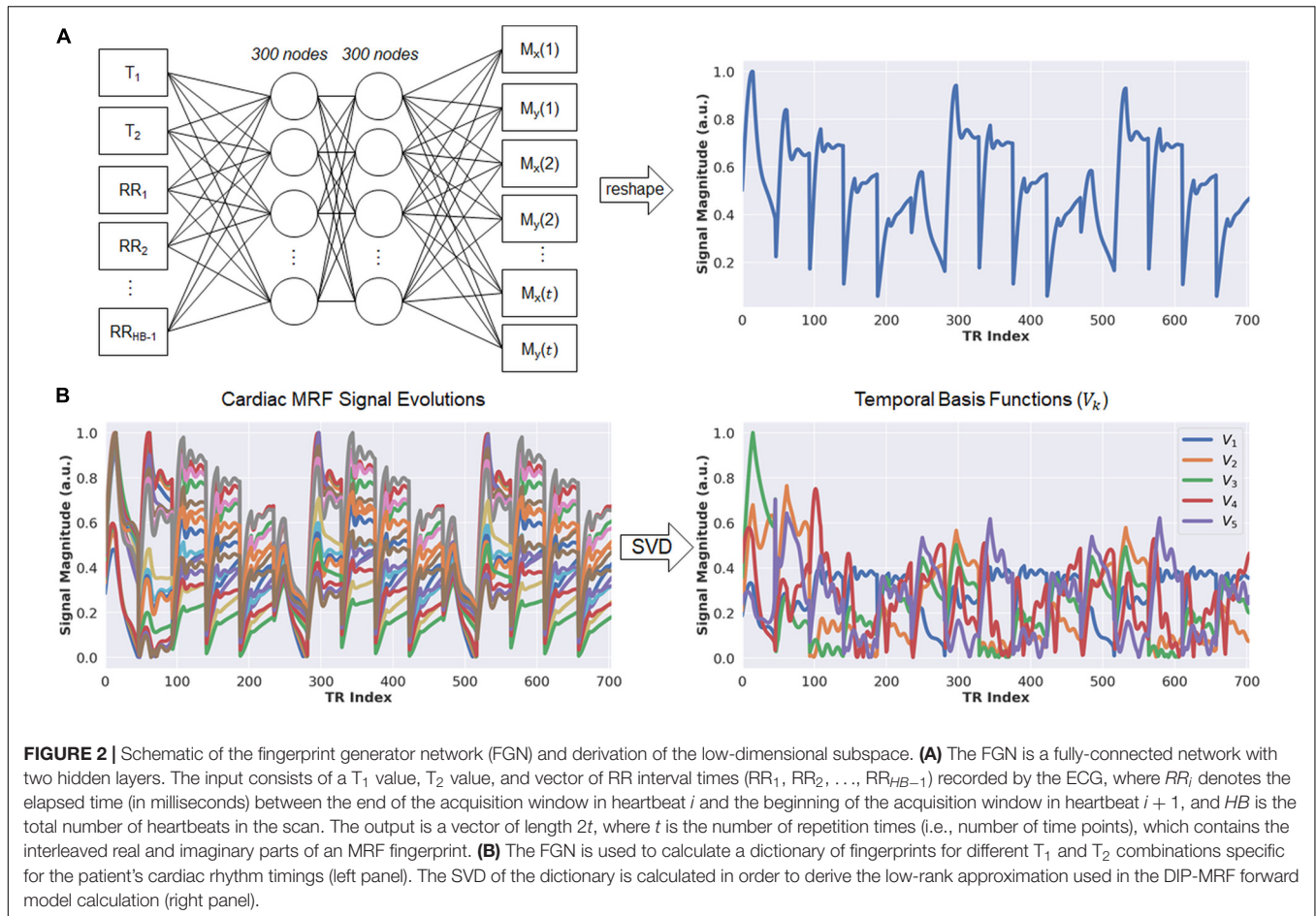
$$x_k = \theta_{IRN}(z) \quad (1)$$

The spatial basis images are multiplied by coil sensitivity maps (S), transformed to k-space by performing an FFT, and multiplied by V_k^* to yield time series data. To reduce memory requirements, a subset of time frames is selected as mini-batch at this point. In practice, this is implemented by using $V_{i,k}^*$ instead of V_k , where $V_{i,k}^*$ denotes the i^{th} column vector from V_k^* (note that multiplication by $V_{i,k}^*$ projects data from the subspace to the time domain and extracts only the i^{th} time frame). The k-space data for time frame i are multiplied by the spiral undersampling mask for the corresponding time frame (P_i) and by the GROG density compensation function (W). The estimated multicoil k-space data for time frame i , denoted by \tilde{y}_i , can be written as,

$$\tilde{y}_i = WP_i \left((FSx_k) V_{i,k}^* \right) \quad (2)$$

The first loss term is calculated as the mean squared error between \tilde{y}_i and the acquired multicoil k-space measurements after density compensation, denoted by y_i , at the sampled locations, and the IRN is updated using backpropagation.

$$\min_{\theta_{IRN}} \sum ||y_i - \tilde{y}_i||_2^2 \quad (3)$$



The PEN is updated in parallel using a second loss term. The T_1 and T_2 maps output by the PEN, along with the subject's RR interval times from the ECG, are input to the FGN to yield simulated fingerprints at each voxel location. These fingerprints are multiplied by the complex-valued M_0 map to obtain a time series of images that are projected onto the subspace by multiplication with V_k . Letting θ_{PEN} and θ_{FGN} denote the network parameters of the PEN and FGN, respectively, the second loss term is calculated as the mean squared error between the resulting images and the spatial basis images output by the IRN:

$$\min_{\theta_{PEN}} \sum ||x_k - (M_0 \theta_{FGN}(T_1, T_2, RR)) V_k||_2^2 \quad (4)$$

For all experiments, training was performed for 30,000 iterations using an Adam optimizer with learning rate 0.001. DIP-MRF was implemented in Tensorflow (v2.8) with Keras on a GPU (NVIDIA Tesla v100 16GB). A mini-batch size of 32 image frames was used to calculate the loss for the IRN.

Cardiac Magnetic Resonance Fingerprinting Acquisition Parameters

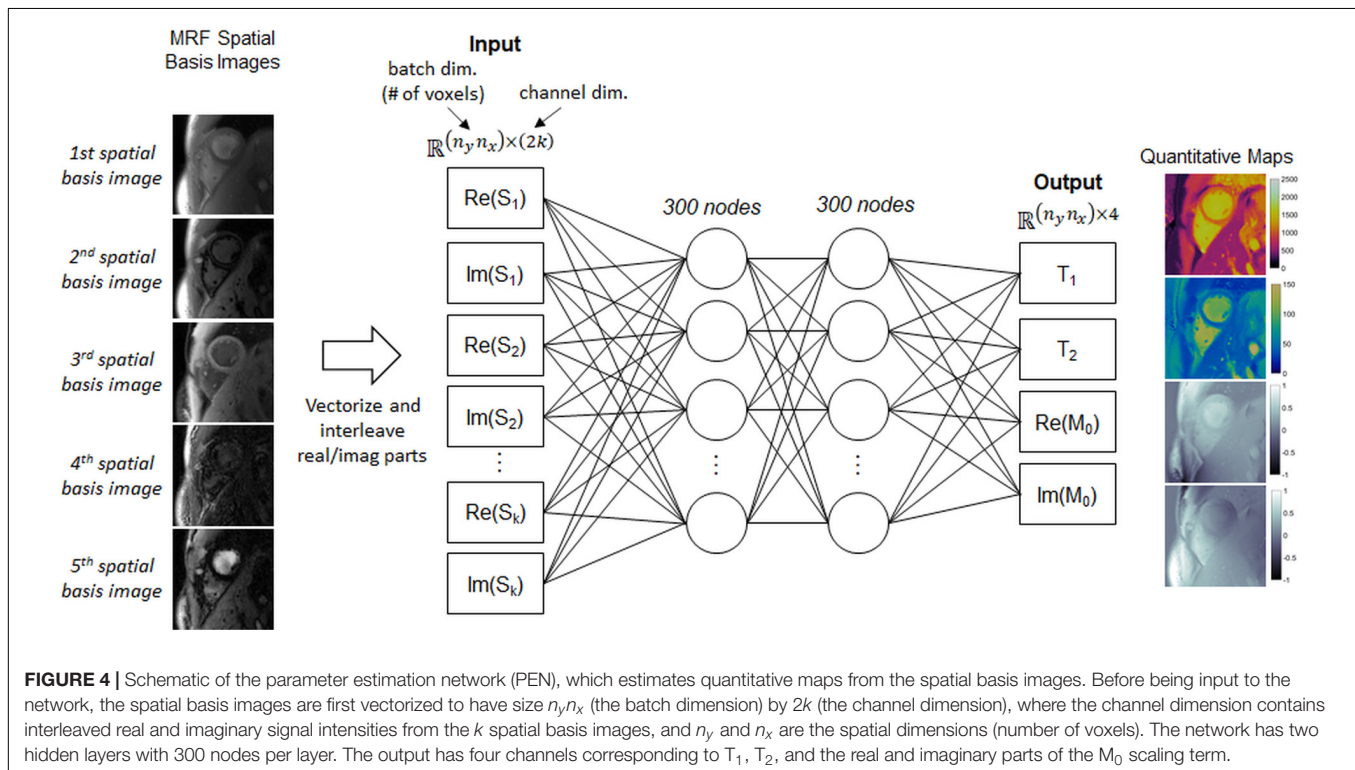
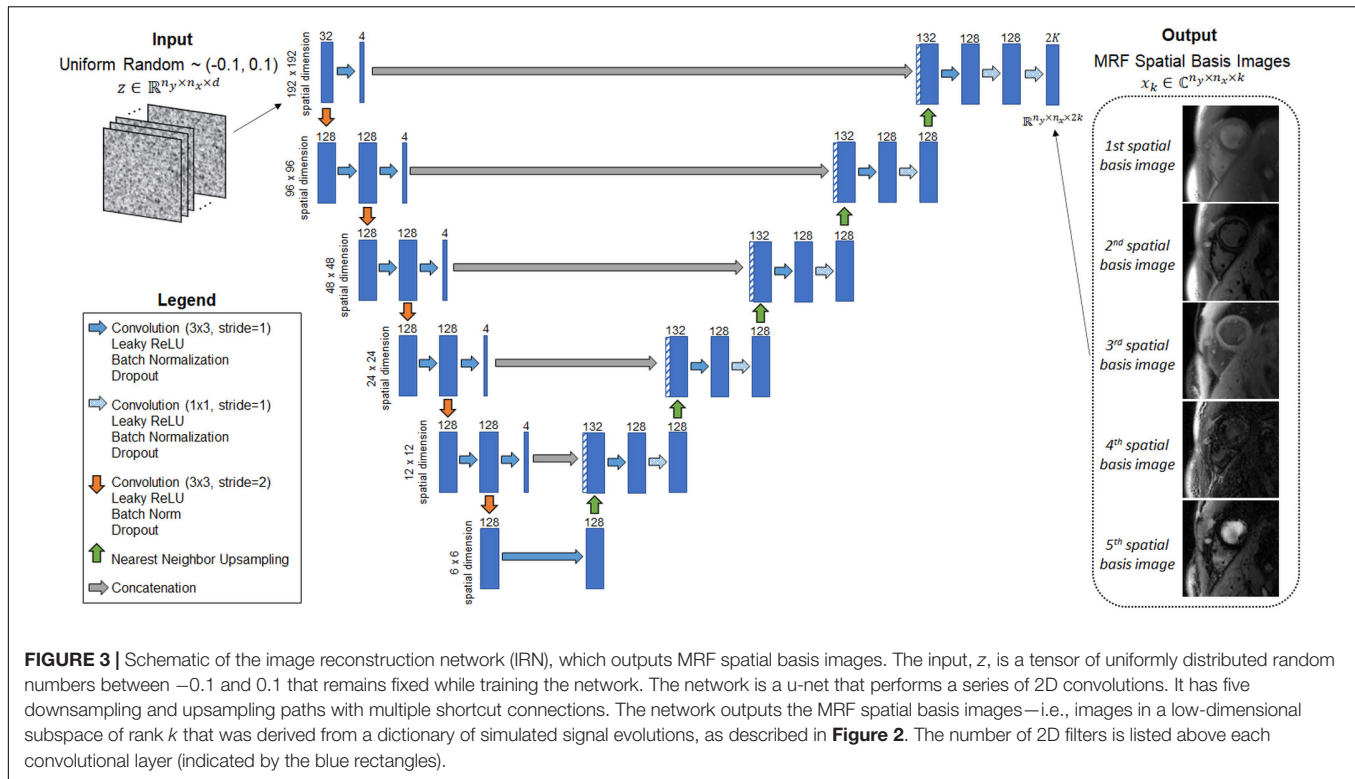
Data were collected using a fast imaging with steady state precession (FISP) cardiac MRF sequence with a 15-heartbeat

(HB) breathhold and 254 ms ECG-triggered diastolic acquisition (15, 40). Variable flip angles ($4-25^\circ$) and a constant TR/TE of 5.4/1.4 ms were employed. A total of 705 undersampled images were collected (one image per TR) with 47 images acquired every heartbeat. Magnetization preparation pulses were applied before the acquisition window in each heartbeat according to the following schedule, which repeated three times during the scan: HB1—inversion (21 ms), HB2—no preparation, HB3— T_2 prep (30 ms), HB4— T_2 prep (50 ms), HB5— T_2 prep (80 ms).

In addition, shortened MRF acquisitions were investigated having a five-heartbeat breathhold and progressively shorter acquisition windows. These were based on the same sequence structure, with the only difference being that the flip angle pattern within each heartbeat was truncated to fit within the desired scan window. An example of a flip angle series for a shortened scan is shown in **Supplementary Figure 2**. All data were acquired using a 48-fold undersampled spiral k-space trajectory (41) with a readout duration of 3.4 ms, matrix size of 192×192 , field-of-view (FOV) of $300 \times 300 \text{ mm}^2$, and golden angle rotation of the trajectory every TR (42).

Simulation Experiments

Simulations were performed to investigate the feasibility of shortening the breathhold and diastolic scan window in cardiac



MRF. In addition to the scan with a 15HB breathhold and 254 ms acquisition window (705 total TRs), scans with a 5HB breathhold and acquisition windows of 254 ms (235 total TRs),

200 ms (185 total TRs), 150 ms (140 total TRs), 100 ms (95 total TRs), and 50 ms (45 total TRs) were simulated. The MRF data acquisition was simulated, including Bloch equation signal

simulation, coil sensitivity encoding with 8-channel sensitivity maps, and spiral k-space undersampling using the NUFFT. Complex Gaussian noise was added to the k-space data having a standard deviation of 0.1% of the maximum amplitude of the direct current (DC) signal. For each sequence variant, maps were reconstructed in three ways. In the first method (*direct matching*), one undersampled image was gridded every TR using the NUFFT, followed by dot product matching with a dictionary generated by a Bloch equation simulation to obtain T_1 , T_2 , and M_0 maps (13). In the second method (*SLLR-MRF*), a sparse and locally low rank MRF reconstruction was performed (34), which yielded a set of $k = 5$ spatial basis images that were matched to an SVD-compressed dictionary. Locally low rank regularization with an 8×8 patch size and l_1 -wavelet regularization were used with regularization weights of $\lambda_{LLR} = 0.02$ and $\lambda_{wav} = 0.005$ relative to the maximum intensity in the basis images. The reconstruction was solved using non-linear conjugate gradient descent with 25 iterations. The third method (*DIP-MRF*) consisted of GROG preprocessing followed by the DIP-MRF reconstruction. The reconstructions were compared using the normalized root mean square error (nRMSE) relative to the ground truth T_1 and T_2 maps, computed over all non-background voxels (i.e., all voxels where the ground truth M_0 was non-zero).

A second set of simulations evaluated the robustness of DIP-MRF to noise. For the sequence with a 5HB breathhold and 150 ms acquisition window, complex Gaussian noise was added to the k-space data having standard deviations (σ_N) of 0, 0.1, 0.2, and 0.3% relative to the maximum amplitude of the DC signal. Maps were reconstructed using direct matching, SLLR-MRF, and DIP-MRF and compared in terms of nRMSE.

A third set of simulations assessed the impact of applying dropout during training (43). For the sequence with a 5HB breathhold and 150 ms acquisition window, the DIP-MRF reconstruction was repeated where different levels of dropout (0, 10, and 20%) were applied after each convolutional layer when training the IRN, and the maps were compared in terms of nRMSE.

Phantom Experiments

Experiments were performed using the ISMRM/NIST MRI system phantom (44) on a 1.5T scanner (MAGNETOM Sola, Siemens Healthineers, Erlangen, Germany). An 8 mm slice was planned through the T_2 layer of the phantom, which has 14 spheres spanning a range of physiological relaxation times with T_1 90–2,230 ms and T_2 10–750 ms. An artificial heart rate of 60 bpm was simulated on the scanner. Data were collected using two cardiac MRF sequences: a sequence with a 15HB breathhold and 254 ms acquisition window and a sequence with a 5HB breathhold and 150 ms acquisition window. Maps were reconstructed using direct matching, SLLR-MRF, and DIP-MRF. Data were also acquired with conventional cardiac mapping sequences using Siemens MyoMaps software (45). T_1 maps were collected with 5(3)3 modified look-locker inversion recovery (MOLLI) (46), and T_2 maps were collected using a 1(3)1(3)1 T_2 -prepared balanced steady state free precession (bSSFP) sequence with T_2 prep times of 0, 25, and 55 ms (5).

Conventional cardiac mapping scans used GRAPPA with an acceleration factor of 2 and 24 autocalibration lines, 6/8 partial Fourier, a flip angle of 35° , and a scan window of 209 ms. All scans were collected with a matrix size of 192×192 and 300 mm^2 FOV. Reference T_1 values were measured using an inversion recovery spin echo sequence with TR = 10 s, TE = 12 ms, and inversion times of 21, 100, 200, 400, 800, and 1,600 ms. Reference T_2 values were measured with a single-echo spin echo sequence with TR = 10 s and echo times of 10, 20, 40, 60, 100, 150, and 200 ms. Mean relaxation times were measured within each vial and compared to reference values using linear regression and Bland-Altman analyses (47). T_2 values above 200 ms were excluded from analysis because the cardiac MRF sequence was not designed for that regime, considering that the longest T_2 prep time was 80 ms (for completeness, measurements in all 14 vials are reported in the **Supplementary Material**).

Scans in Healthy Subjects and Patients

Eighteen healthy subjects were scanned at 1.5T after obtaining written informed consent in this IRB-approved, HIPAA-compliant study. All scans were performed during an end-expiratory breathhold at a mid-ventricular slice position. MOLLI and T_2 -prep bSSFP mapping were performed in all subjects. Data were also acquired using 15HB/254 ms and 5HB/150 ms cardiac MRF acquisitions, and maps were reconstructed using direct matching, SLLR-MRF, and DIP-MRF. To study the effects of training with dropout and to determine the optimal dropout percentage, the DIP-MRF reconstruction was repeated in three subjects with 0, 5, 10, 20, and 30% dropout applied after each convolutional layer when training the IRN. Unless otherwise stated, the DIP-MRF reconstruction used dropout levels of 10 and 20% for the 15HB/254 ms and 5HB/150 ms MRF acquisitions, respectively.

In addition, data were collected in ten patients referred for a clinical CMR exam due to suspected cardiomyopathy. Native T_1 and T_2 maps were collected using the same protocol as in healthy subjects. Post-contrast T_1 and T_2 maps were acquired 15–25 min after IV injection of 0.2 mmol/kg body weight gadoteridol (ProHance, Bracco Diagnostics Inc., Princeton, NJ, United States). While post-contrast MRF scans (both 15HB/254 ms and 5HB/150 ms versions) were performed in all patients, post-contrast MOLLI and T_2 -prep bSSFP sequences were only collected in nine and three patients, respectively.

In vivo data were analyzed by manually segmenting the maps according to American Heart Association (AHA) guidelines (48). The mean and standard deviation for T_1 and T_2 were measured within each AHA segment and over all voxels in the myocardium. Similarly, T_1 and T_2 values were measured within the left (LV) and right ventricular (RV) blood pools after manual segmentation, taking care to avoid trabeculations and papillary muscles. Intersubject variability was quantified as the standard deviation of the mean T_1 or T_2 values over all subjects. Intrasubject variability was quantified by measuring the standard deviation in T_1 or T_2 for each subject and then calculating the mean over all subjects. T_1 and T_2 measurements using different reconstruction methods within the same subject were compared

using a within-subjects ANOVA test with a Bonferroni *post-hoc* test for multiple comparisons, with $p < 0.05$ indicating statistical significance, as well as Bland-Altman plots. T_1 and T_2 measurements between healthy subjects and patients were compared using a two-sample *t*-test.

RESULTS

Simulation Experiments

Figure 5A shows simulation results using MRF sequences with different breathhold and acquisition window lengths. In all cases, the nRMSE was highest with direct matching and lowest with DIP-MRF, and this difference was more pronounced for shorter sequence lengths. As the breathhold and acquisition window were shortened, nRMSE increased for direct matching and SLLR-MRF but remained consistently low for DIP-MRF. For the 15HB/254 ms sequence, the nRMSE was (T_1 6.5%, T_2 11.2%) for direct matching, (T_1 2.9%, T_2 4.3%) for SLLR-MRF, and (T_1 1.4%, T_2 0.7%) for DIP-MRF. For the 5HB/150 ms sequence, the nRMSE was (T_1 13.4%, T_2 20.2%) for direct matching, (T_1 6.4%, T_2 9.1%) for SLLR-MRF, and (T_1 1.2%, T_2 0.8%) for DIP-MRF. **Supplementary Figure 3** shows examples of T_1 , T_2 , and M_0 maps from the simulation study.

Figure 5B plots the nRMSE for the 5HB/150 ms sequence as the *k*-space data were corrupted with different amounts of complex Gaussian noise. The nRMSE was highest with direct matching and lowest with DIP-MRF at all noise levels. At the highest noise level tested ($\sigma_N = 0.3\%$ of the DC signal), the nRMSE was (T_1 14.9%, T_2 22.5%) for direct matching, (T_1 10.0%, T_2 14.6%) for SLLR-MRF, and (T_1 1.5%, T_2 0.9%) for DIP-MRF.

Supplementary Figure 4 demonstrates the importance of applying dropout in DIP-MRF, with simulation results shown for the 5HB/150 ms sequence. Without dropout, the nRMSE reached a minimum (T_1 1.7%, T_2 1.0%) after approximately 5,000 iterations. The nRMSE increased gradually with further training due to overfitting to noise and undersampling artifacts, reaching (T_1 2.2%, T_2 1.4%) after 30,000 iterations. Using dropout improved the reconstruction accuracy, as the minimum nRMSE was lower compared to the 0% dropout case, and it reduced overfitting, allowing the network to be trained for longer without causing the nRMSE to increase. For example, with 20% dropout, the nRMSE reached a minimum of (T_1 1.5%, T_2 0.8%) after 12,000 iterations and only increased slightly to (T_1 1.7%, T_2 1.0%) after 30,000 iterations.

Phantom Experiments

Bland-Altman plots showing the agreement between 15HB/254 ms MRF, 5HB/150 ms MRF, and conventional mapping sequences relative to reference values are shown in **Figure 6**; linear regression plots of the same data are shown in **Supplementary Figure 5**, and T_2 measurements in all 14 vials (including vials with $T_2 > 200$ ms) are given in **Supplementary Figures 6, 7**. There were no significant differences in T_1 or T_2 relative to reference values for all MRF methods. Using DIP-MRF, the bias and 95% limits of agreement (LoA) for T_1 were 4 ms (−45, 52)ms for the 15HB/254 ms sequence and

−5 ms (−61, 51) ms for the 5HB/150 ms sequence; for T_2 , they were −0.9 ms (−5.5, 3.7) ms for the 15HB/254 ms sequence and 0.2 ms (−3.1, 3.4) ms for the 5HB/150 ms sequence. In general, DIP-MRF yielded narrower limits of agreement compared to direct matching and SLLR-MRF. MOLLI slightly underestimated T_1 with a bias of −39 ms and 95% LoA of (−86, 8) ms. T_2 -prep bSSFP overestimated T_2 with a bias of 35.6 ms and 95% LoA of (−45.9, 117.2) ms. This overestimation was larger for vials with short T_2 values below approximately 100 ms, which is apparent on the linear regression plots (**Supplementary Figure 5**). The correlation coefficients were similar among all reconstructions for the 15HB/254 ms MRF sequence, with all $R^2 > 0.998$. For the 5HB/150 ms sequence, the correlation was slightly higher for DIP-MRF ($R^2 = 0.999$ for T_1 , $R^2 = 1.000$ for T_2) compared to direct matching ($R^2 = 0.998$ for T_1 , $R^2 = 0.995$ for T_2) and SLLR-MRF ($R^2 = 0.998$ for T_1 , $R^2 = 0.999$ for T_2).

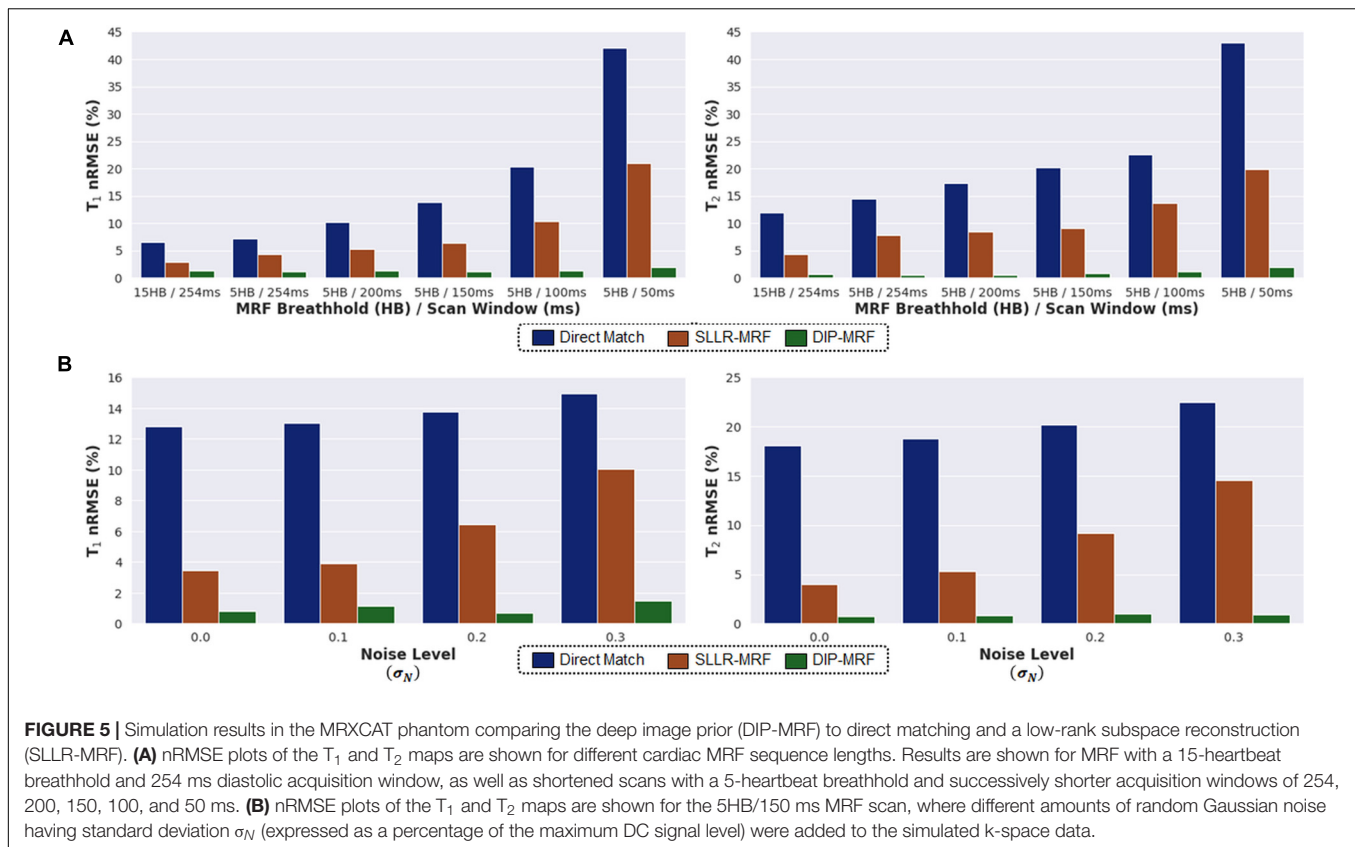
Scans in Healthy Subjects

Representative maps in a healthy subject using 15HB/254 ms MRF, 5HB/150 ms MRF, and conventional mapping sequences are shown in **Figure 7**. Additional examples are provided in **Supplementary Figures 8–10**. Some noise enhancement was observed with direct matching for the 15HB/254 ms MRF sequence, with better map quality using SLLR-MRF and DIP-MRF reconstructions. The improvement using DIP-MRF was especially pronounced for the 5HB/150 ms sequence; direct matching led to severe noise enhancement and aliasing artifacts, SLLR-MRF provided only moderate noise suppression, and DIP-MRF gave the best suppression of noise and aliasing artifacts while preserving high resolution details, such as the papillary muscles.

Figure 8 shows examples of spatial basis images from DIP-MRF compared to those from conventional NUFFT gridding and SLLR-MRF. Noise enhancement was observed with NUFFT gridding, especially for the 4th and 5th basis images, which was partially reduced using SLLR-MRF, with DIP-MR yielding the best image quality.

Figure 9 demonstrates the effect of training DIP-MRF with different levels of dropout, akin to the simulation results in **Supplementary Figure 4**. From a visual inspection of the maps, the dropout level that yielded the best noise suppression while preserving high resolution details was 10% for the 15HB/254 ms sequence and 20% for the 5HB/150 ms sequence, when the number of training iterations was fixed at 30,000. Noise enhancement and residual aliasing artifacts were observed at lower dropout levels, whereas overly smoothed maps with loss of fine resolution details were seen at higher dropout levels. Results in two additional subjects are shown in **Supplementary Figures 11, 12**.

Boxplots summarizing the average relaxation times over all subjects in the myocardial septum are shown in **Figure 10**. T_1 values reported as mean \pm standard deviation were: MOLLI ($1,006 \pm 28$ ms); 15HB/254 ms MRF with direct matching ($1,043 \pm 36$ ms), SLLR-MRF ($1,064 \pm 42$ ms), and DIP-MRF ($1,044 \pm 33$ ms); and 5HB/254 ms MRF with direct matching ($1,065 \pm 53$ ms), SLLR-MRF ($1,072 \pm 39$ ms), and DIP-MRF ($1,035 \pm 32$ ms). T_2 values were: T_2 -prep bSSFP (47.7 ± 1.6 ms);



15HB/254 ms MRF with direct matching (40.8 ± 3.0 ms), SLLR-MRF (42.3 ± 3.0 ms), and DIP-MRF (41.3 ± 2.9 ms); and 5HB/254 ms MRF with direct matching (46.1 ± 9.0 ms), SLLR-MRF (44.5 ± 3.9 ms), and DIP-MRF ($43. \pm 3.8$ ms). T_1 was significantly higher with all MRF techniques compared to MOLLI. T_2 was significantly lower with all MRF techniques compared to T_2 -prep bSSFP, except for the 5HB/150 ms sequence with direct matching. A similar analysis of relaxation times in LV and RV blood is given in **Supplementary Figure 14**.

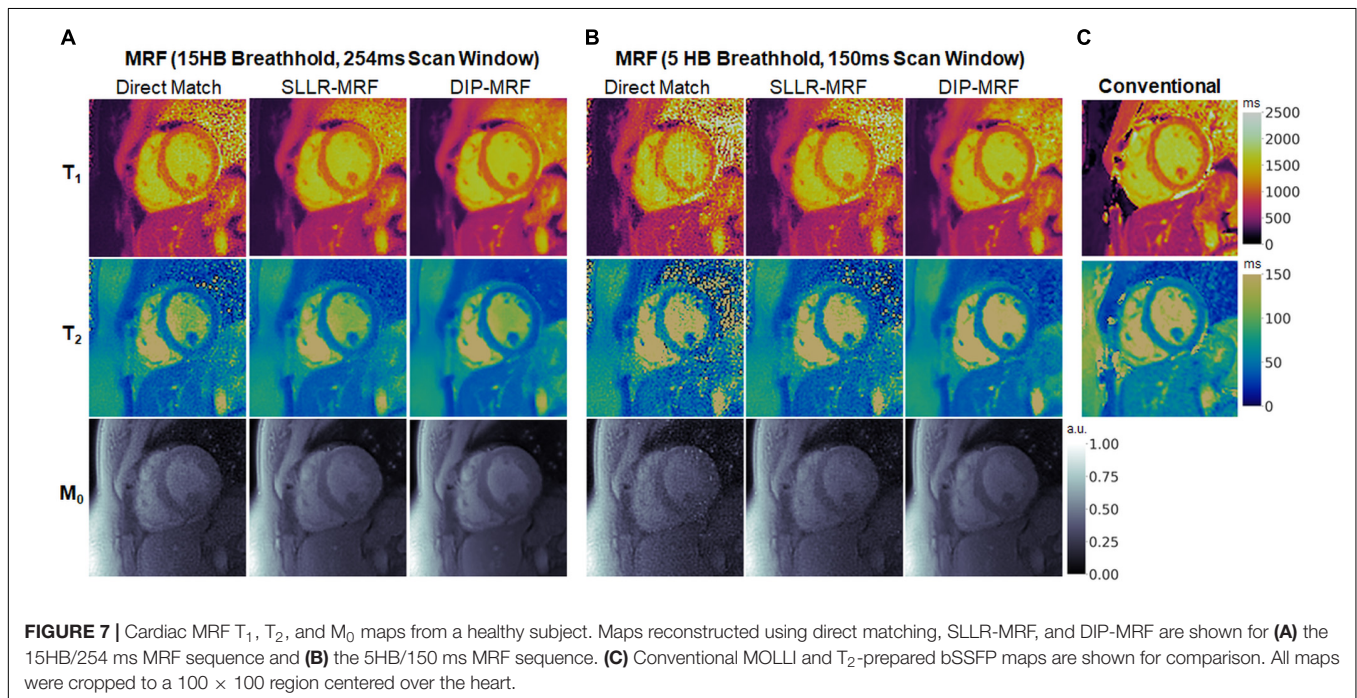
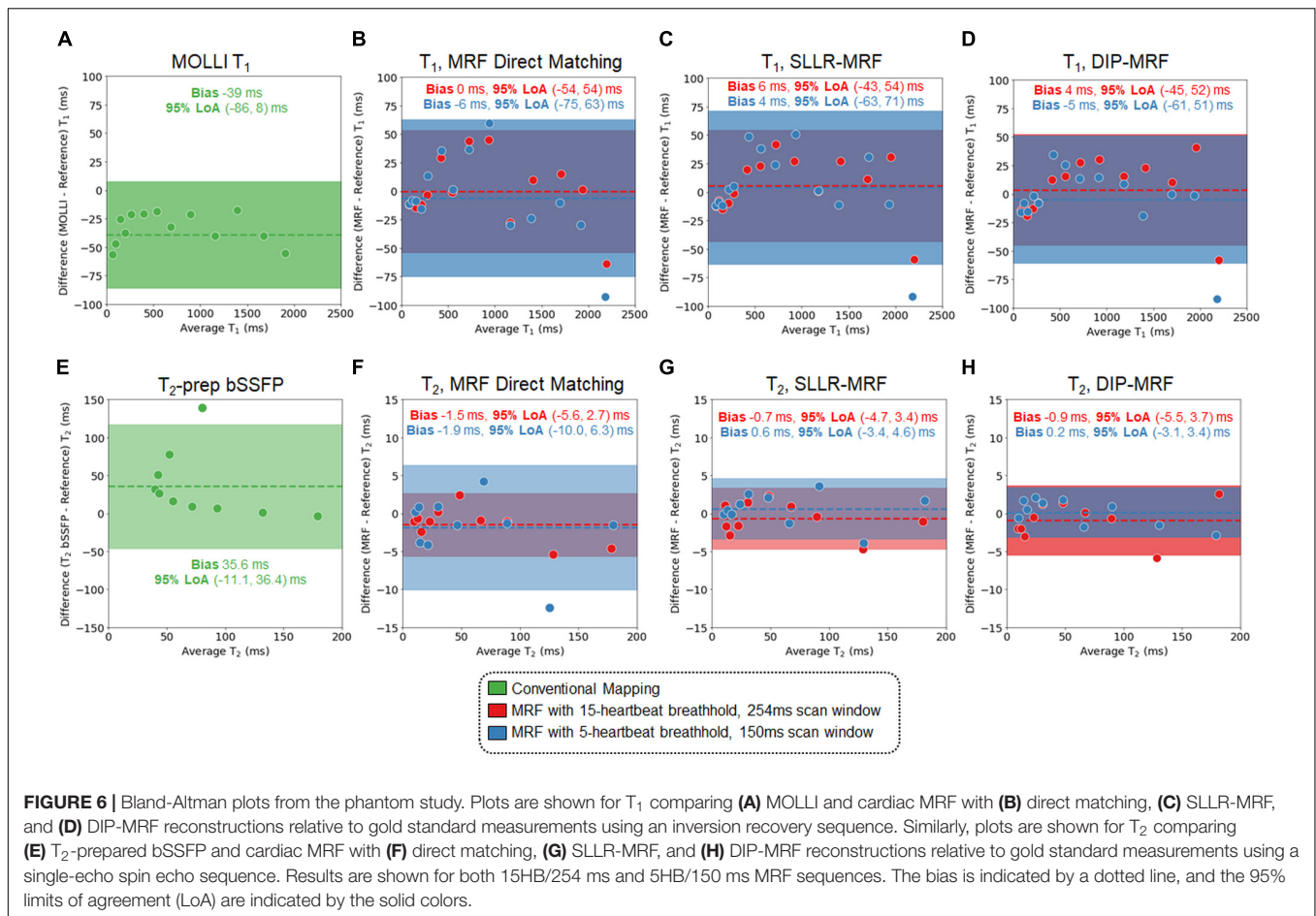
The intersubject variability, quantified as the standard deviation of the mean T_1 or T_2 over all subjects, was similar among all reconstructions for the 15HB/254 ms MRF scan. For the 5HB/150 ms scan, DIP-MRF yielded a lower intersubject variability (32 ms for T_1 , 3.8 ms for T_2) compared to direct matching (53 ms for T_1 , 9.0 ms for T_2) and SLLR-MRF (39 ms for T_1 , 3.9 ms for T_2), although still higher than conventional mapping sequences (28 ms for T_1 , 1.5 ms for T_2).

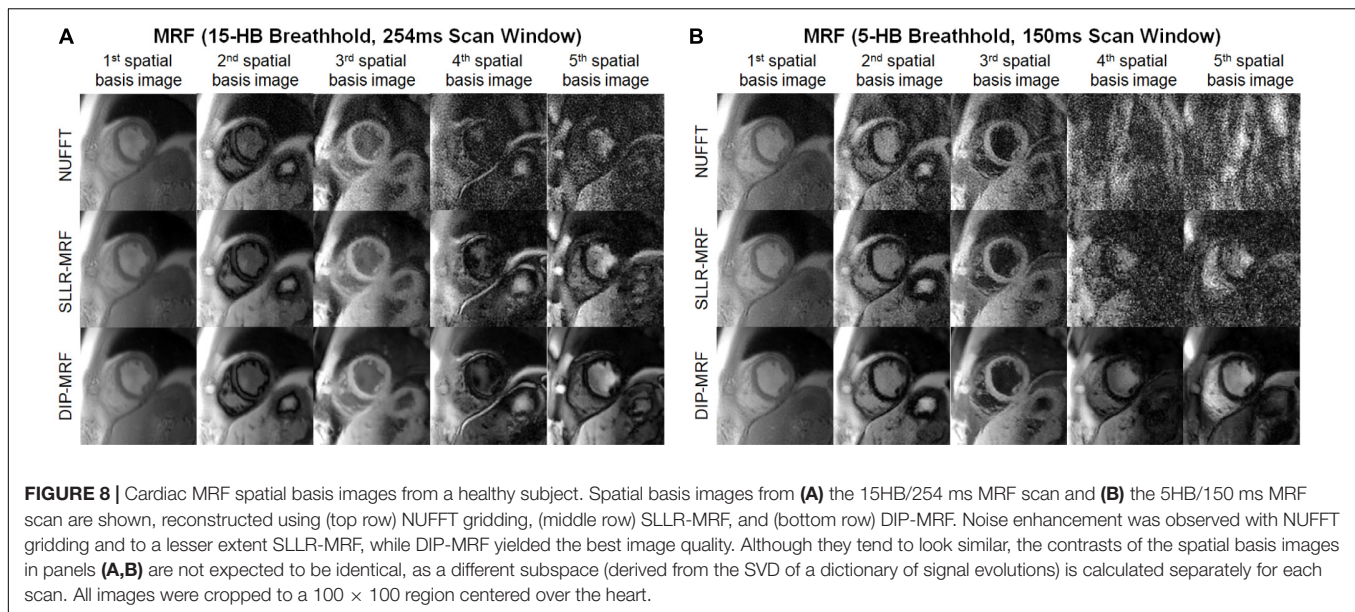
Bland-Altman plots comparing relaxation times measured with 15HB/254 ms vs. 5HB/150 ms MRF scans are shown in **Figure 11** (note that a positive bias indicates higher measurements using the 5HB/150 ms scan). Both scans yielded good agreement in T_1 when using the DIP-MRF reconstruction, with a bias of -9 ms and 95% LoA ($-56, 38$) ms. Similar results were seen with SLLR-MRF, having a bias of 8 ms and 95% LoA ($-41, 58$) ms, while a larger bias (22 ms) and wider limits of agreement of ($-81, 206$) ms were observed with direct matching. DIP-MRF yielded the best agreement between T_2 measurements

from the 15HB/254 ms and 5HB/150 ms scans, with a bias of 2.0 ms and 95% LoA ($-1.9, 6.0$) ms. SLLR-MRF had a similar bias (2.1 ms) but wider limits of agreement of ($-3.4, 7.7$) ms. Direct matching had the largest bias (5.3 ms) and widest limits of agreement ($-8.7, 19.4$) ms.

Figures 12A,B show the spatial distribution of T_1 and T_2 within individual myocardial segments and over the entire myocardium. Both 15HB/254 ms and 5HB/150 ms MRF scans showed some regional variability in T_1 and T_2 , with higher values in the septum and lower values in the inferolateral segment. A similar but less pronounced trend was seen with MOLLI but not with T_2 -prepared bSSFP. Greater regional variability was seen with direct matching compared to SLLR-MRF and DIP-MRF.

Figures 12C,D summarize the intrasubject variability for T_1 and T_2 , quantified as the mean of the standard deviations over all subjects, shown within each myocardial segment and over the entire myocardium. Compared to MOLLI (57 ms), the intrasubject variability in T_1 over the entire myocardium was significantly higher using the 15HB/254 ms MRF sequence with direct matching (94 ms); this variability was reduced with SLLR-MRF (66 ms) and DIP-MRF (57 ms) and was not significantly different from MOLLI. For the 5HB/150 ms MRF sequence, the intrasubject variability was significantly higher than MOLLI when using direct matching (160 ms) and SLLR-MRF (86 ms); DIP-MRF yielded the lowest variability (61 ms) with no significant difference relative to MOLLI. Compared to T_2 -prep bSSFP (4.2 ms), the intrasubject variability in T_2 over





the entire myocardium using the 15HB/254 ms MRF sequence was significantly higher using direct matching (5.6 ms), non-significantly lower using SLLR-MRF (3.9 ms), and significantly lower using DIP-MRF (3.3 ms). For the 5HB/150 ms MRF sequence, the intrasubject variability was significantly higher than T_2 -prep using direct matching (19.1 ms) and SLLR-MRF (7.1 ms); DIP-MRF yielded the lowest variability (4.1 ms) with no significant difference relative to T_2 -prep bSSFP.

Patient Scans

Representative maps from a cardiomyopathy patient are shown in **Figure 13**, with additional patient examples provided in **Supplementary Figures 15, 16**. In both native and post-contrast maps in patients, DIP-MRF yielded the best suppression of noise and aliasing artifacts, especially for the shortened 5HB/150 ms acquisition, where direct matching led to severe noise and artifacts that were only moderately improved with the SLLR-MRF reconstruction.

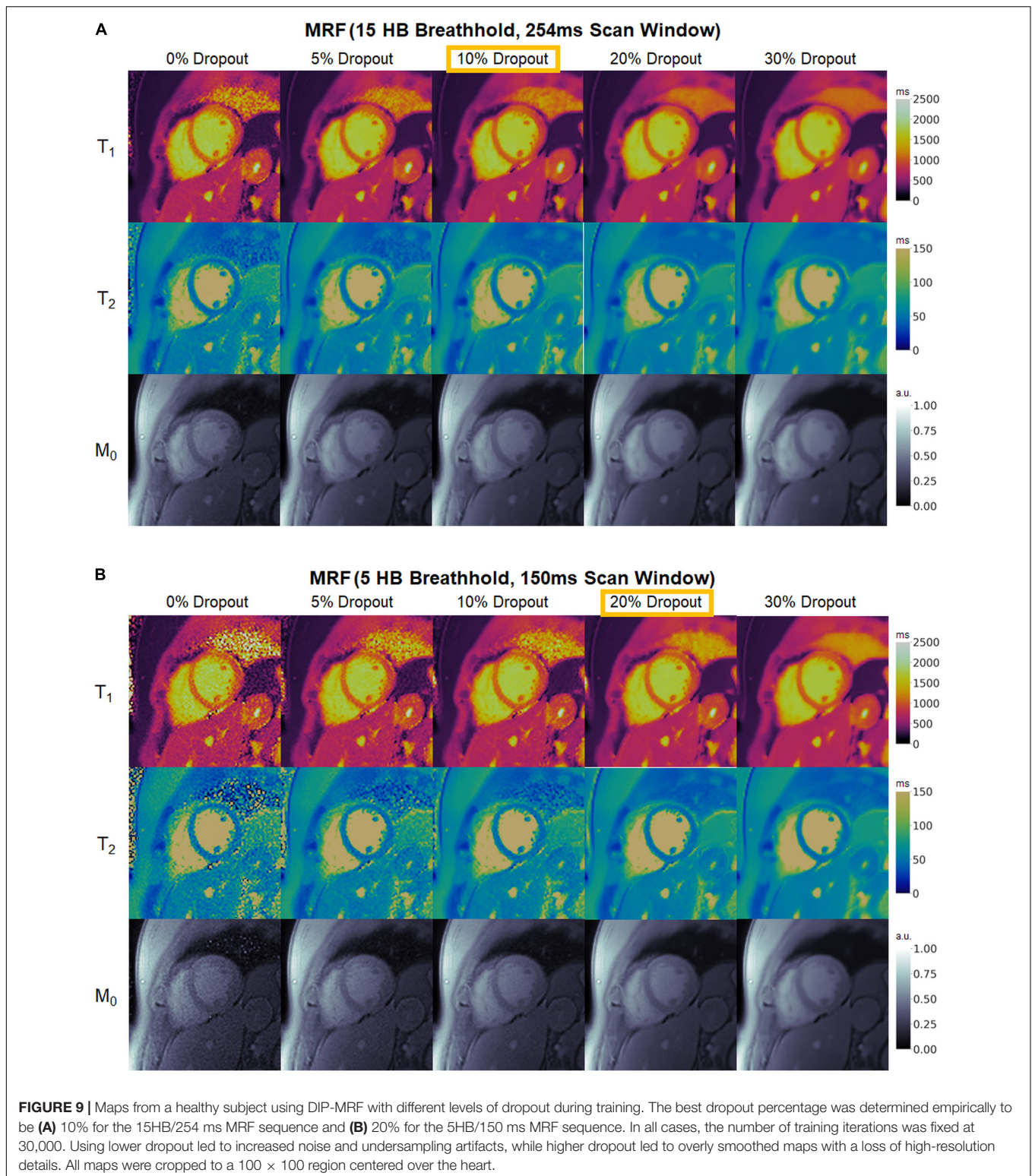
Figure 14 shows one example of a patient scan where the 15HB breathhold and 254 ms acquisition window resulted in motion artifacts. In this case, motion caused blurring of the myocardial wall and an artifactual increase in septal relaxation times due to partial volume effects between myocardium and blood, with DIP-MRF yielding T_1 1263 ± 48 ms and T_2 55.8 ± 6.5 ms. To confirm the presence of motion, a sliding window reconstruction was performed (window size = 48 TRs) to visualize one image per heartbeat, shown in **Supplementary Figure 17**. This analysis confirmed that the patient breathed halfway during the scan, and residual cardiac motion was apparent in the later heartbeats. Motion and partial volume effects were reduced using the shorter 5HB breathhold and 150 ms acquisition window, leading to a sharper depiction of the myocardial wall and lower septal relaxation times of T_1 1130 ± 27 ms and T_2 48.8 ± 4.1 ms (although T_1 and T_2 were still elevated compared to healthy subjects). Conventional

MOLLI and T_2 -prep bSSFP mapping values in this patient were $T_1 = 1,122 ± 47$ ms and $T_2 = 50.1 ± 4.1$ ms.

Boxplots summarizing the distribution of native and post-contrast relaxation times in the myocardial septum in patients are shown in **Figure 15**. Using the DIP-MRF reconstruction, both 15HB/254 ms MRF (1,079 ± 72 ms) and 5HB/150 ms MRF (1,047 ± 46 ms) acquisitions yielded higher native T_1 than MOLLI (1,033 ± 34 ms); this difference was statistically significant for 5HB/150 ms DIP-MRF. Native T_2 was non-significantly lower with both 15HB/254 ms MRF (45.2 ± 5.8 ms) and 5HB/150 ms MRF (45.7 ± 4.0 ms) compared to T_2 -prep bSSFP (47.6 ± 3.9 ms). Patients had higher native T_1 than healthy subjects, but this trend was not significant for MOLLI, 15HB/254 ms MRF, or 5HB/150 ms MRF. Compared to healthy subjects (45.2 ms), native T_2 in patients was significantly lower with 15HB/254 ms MRF (41.3 ms) and non-significantly lower with 5HB/150 ms MRF (43.3 ms). No difference between patients and healthy subjects was seen with T_2 -prep bSSFP (47.6 vs. 47.7 ms). There were no significant differences in post-contrast T_1 among MOLLI (417 ± 38), 15HB/254 ms MRF (409 ± 62 ms), or 5HB/150 ms MRF (397 ± 51 ms). Post-contrast myocardial T_2 was 37.9 ± 3.0 ms using 15HB/254 ms MRF and 38.7 ± 3.5 ms using 5HB/150 ms MRF (**Supplementary Figure 18**). Post-contrast T_2 bSSFP data were only acquired in a subset of three patients; a comparison of post-contrast T_2 bSSFP and MRF in these patients is provided in **Supplementary Table 1**. An analysis of native and post-contrast relaxation times in LV and RV blood in patients is given in **Supplementary Figure 19**.

DISCUSSION

This study introduced a self-supervised deep learning reconstruction for cardiac MRF, called DIP-MRF, that combines low-rank subspace modeling with the denoising



capabilities of a deep image prior. DIP-MRF was shown to reduce noise and aliasing artifacts in tissue property maps compared to conventional dictionary matching and a low-rank subspace reconstruction with spatial and locally low rank

constraints (SLLR-MRF). DIP-MRF was leveraged to shorten the breathhold duration of cardiac MRF from 15 to 5 heartbeats and the diastolic acquisition from 250 to 150 ms *in vivo*, which can potentially reduce motion artifacts, especially for

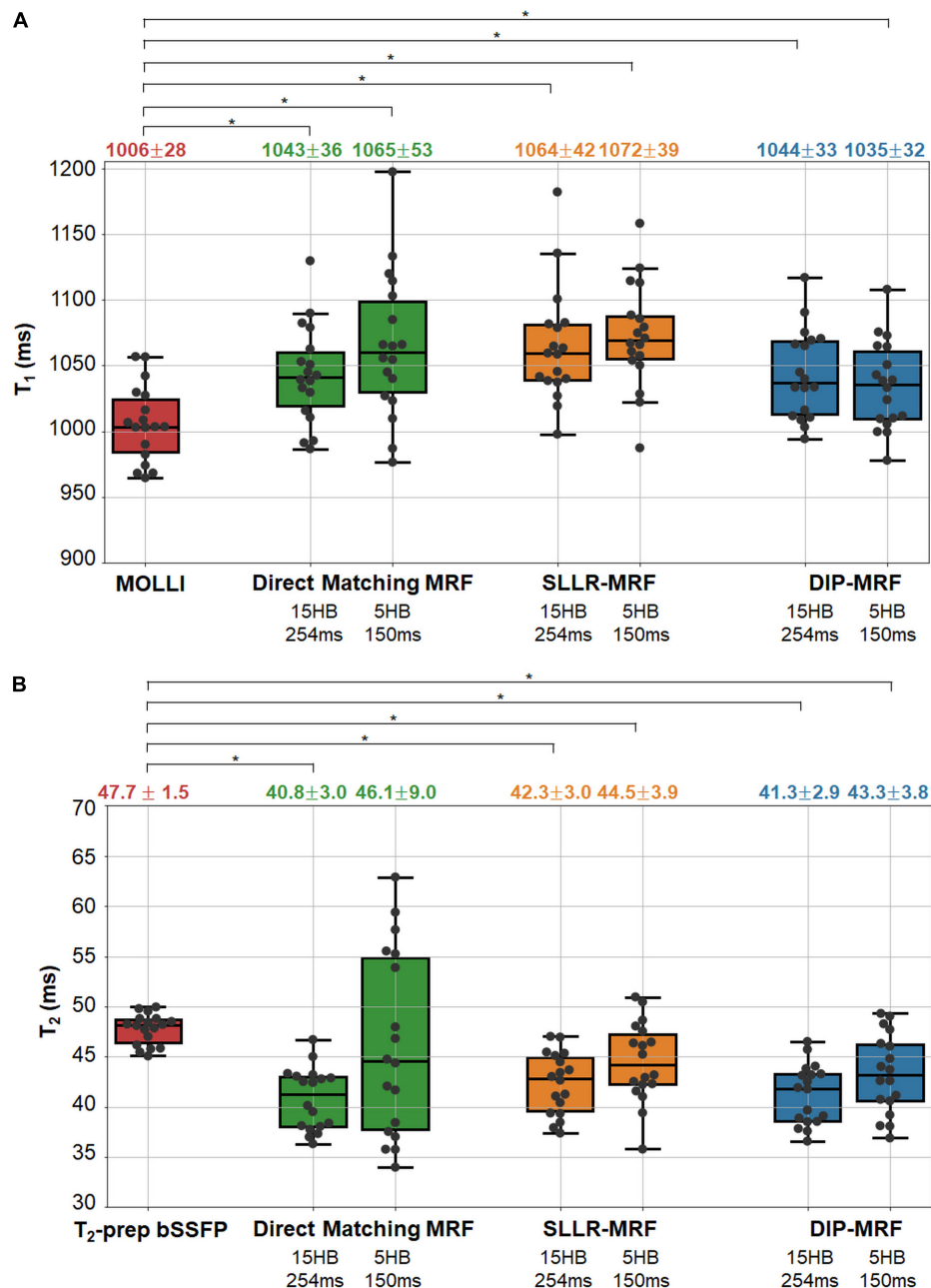
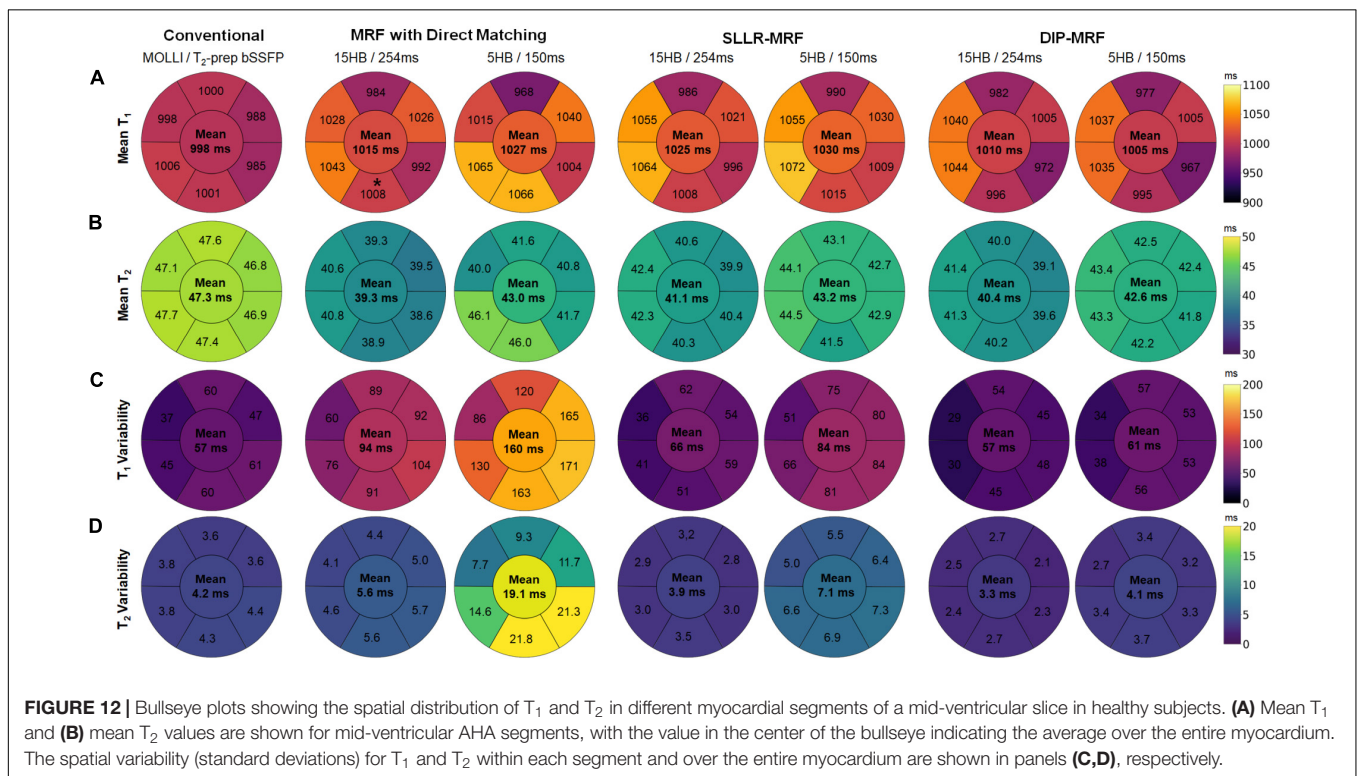
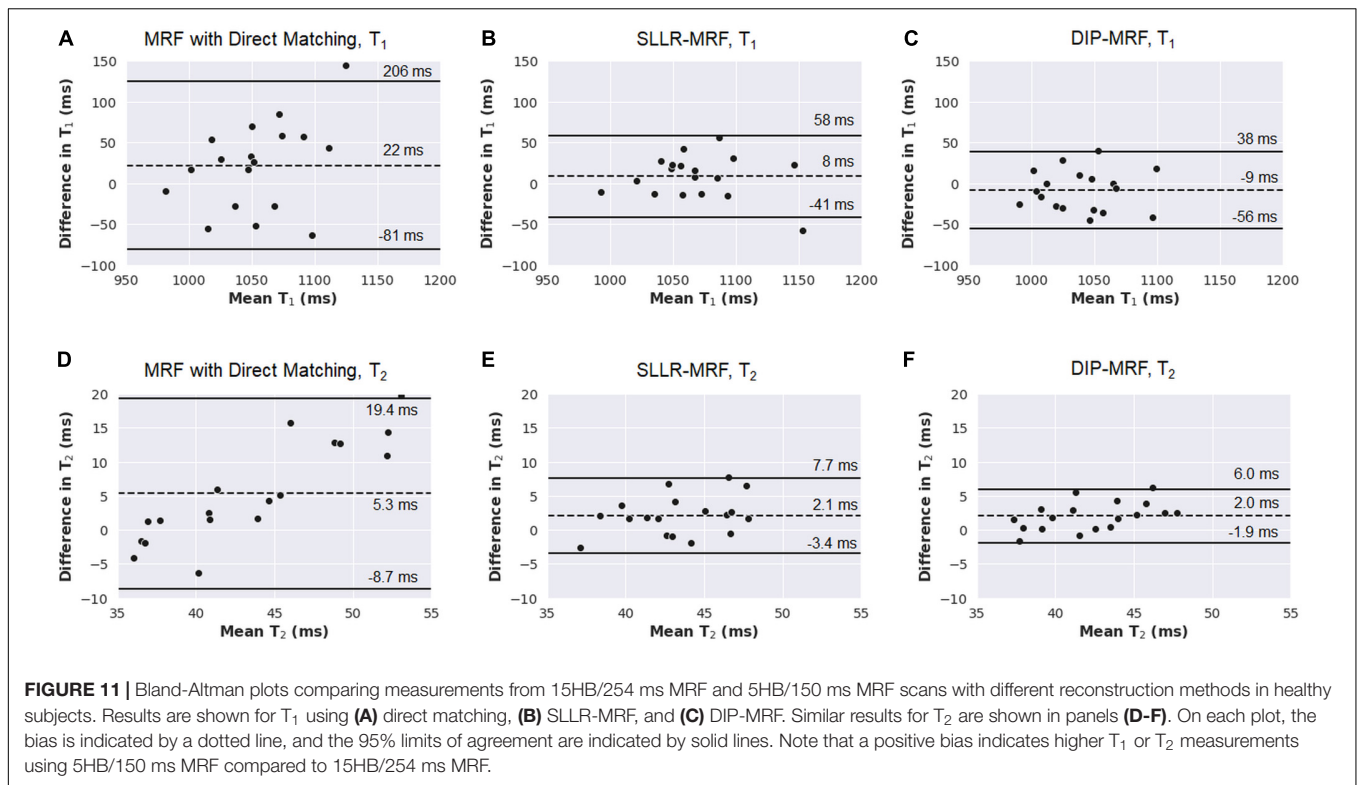


FIGURE 10 | Myocardial T_1 and T_2 in healthy subject in the left ventricular septum. The boxplots show the distribution of mean (A) T_1 and (B) T_2 values using MOLLI and T_2 -prep bSSFP mapping sequences, as well as 15HB/254 ms and 5HB/150 ms MRF sequences with direct matching, SLLR-MRF, and DIP-MRF reconstructions. The top of each box indicates the upper quartile, the bottom indicates the lower quartile, and the horizontal line through the middle shows the median. The numbers above each plot indicate the mean \pm standard deviation in milliseconds. Asterisks indicate a significant difference ($p < 0.05$) using a within-subjects ANOVA test with a Bonferroni *post-hoc* test for multiple comparisons.

patients who have difficulty performing long breathholds or who have elevated heart rates. By minimizing motion, the shortened acquisition may also decrease partial volume artifacts between myocardium and blood, leading to more accurate and reproducible myocardial T_1 and T_2 measurements. This effect was demonstrated in **Figure 14**, where motion resulted in an artifactual increase in myocardial T_1 and T_2 with the longer

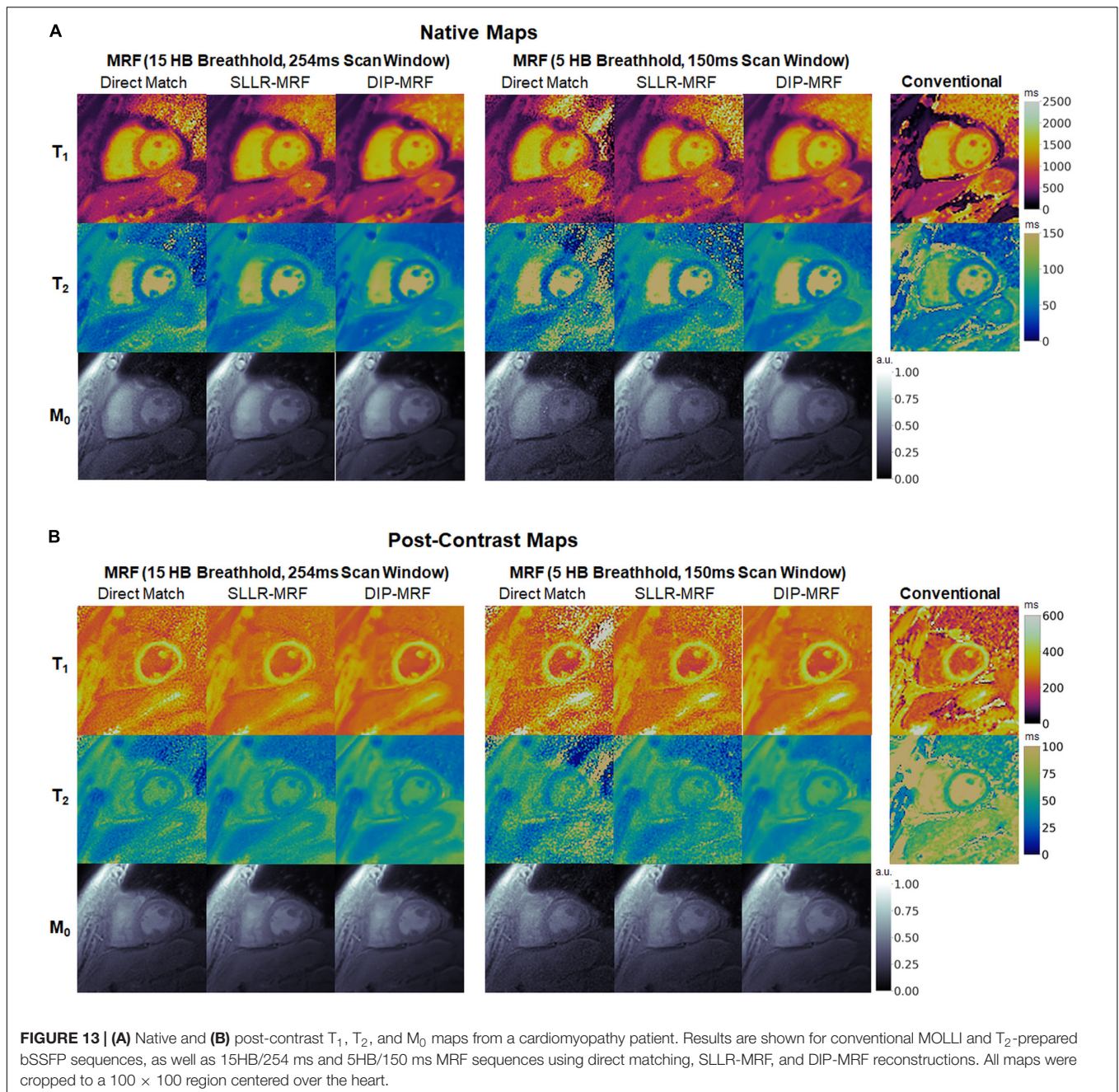
MRF scan that was mitigated by shortening the breathhold and scan window.

In most deep learning reconstructions, a neural network is pre-trained using a large number of reference images. For MRE, such training data would consist of “ground truth” tissue property maps (the network output) paired with a time series of undersampled images or k-space measurements (the network



input). While it is possible to collect such training data in stationary organs, like the brain, it is more challenging in the heart due to physiological motion and the long scan times that

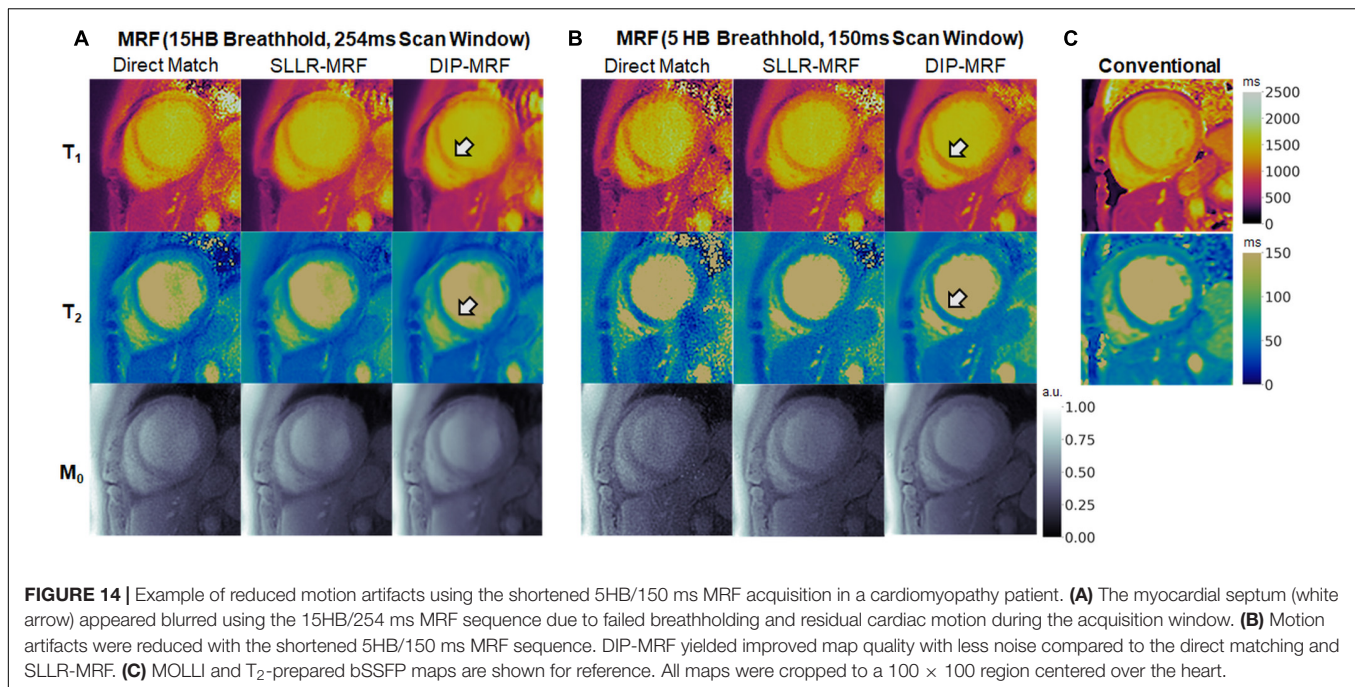
would be required to collect fully-sampled MRF data (on the order of several minutes). Additionally, the fingerprints in cardiac MRF are dependent on the subject's cardiac rhythm because the



scan uses prospective ECG triggering, so many datasets would potentially be needed to ensure the network provides accurate tissue property estimates independent of a patient's cardiac rhythm. DIP-MRF addresses these challenges by eliminating the need for prior training. Instead, training is performed *de novo* after each MRF acquisition, and the only requirements for training data are the undersampled k-space measurements from the current scan and the patient's cardiac rhythm timings from the ECG. The self-supervised training used in DIP-MRF ensures that the reconstructed T_1 , T_2 , and M_0 maps and spatial basis images are consistent with the acquired k-space data and with

a mathematical model of the MRF signal generation and data sampling process.

One limitation of this work is the long computation time of approximately 1.1 h, since training is performed *de novo* for each scan. Nevertheless, this work used strategies to accelerate the calculation of forward model during training. The spiral k-space data were shifted onto a Cartesian grid using GROG, which allowed use FFT rather than more time-consuming NUFFT operations during training. Without GROG pre-interpolation, the DIP-MRF reconstruction took 5.3 h. A pre-trained Fingerprint Generator Network was also used in place of



a Bloch equation simulation to rapidly generate fingerprints for arbitrary T_1 , T_2 , and cardiac rhythm timings. The time needed to simulate fingerprints at 192^2 voxel locations (the matrix size used for all datasets in this work) was over 8 min using a Bloch simulation (compiled MATLAB Mex code running on 12 parallel CPUs) compared to 30 ms using the Fingerprint Generator Network on a GPU. Future work will explore ways to shorten the computation time of DIP-MRF, possibly to several minutes or less. Transfer learning may be one solution (49), where DIP-MRF is pre-trained using some *in vivo* scans, and the reconstructed maps are fine-tuned based on the acquired k-space data from the current scan.

In the original DIP publication, early stopping was used to avoid overfitting to noise, and the number of training iterations was manually tuned for each application (27). This study uses dropout to reduce overfitting (43), which allowed the network to be trained for longer and placed less dependence on manually tuning the number of iterations for early stopping. Simulation results showed that dropout improved the reconstruction accuracy and slowed the rate at which overfitting occurred (**Supplementary Figure 4**). An *in vivo* dataset was also reconstructed with different dropout levels, while keeping the number of training iterations fixed at 30,000 for simplicity, to empirically determine which settings yielded the best map quality. It was found that the shortened 5HB/150 ms MRF scan benefitted from higher dropout compared to the 15HB/254 ms scan (20 vs. 10% dropout).

In the absence of motion, the 15HB/254 ms and 5HB/150 ms MRF sequences were expected to yield equivalent T_1 and T_2 measurements. However, large differences were observed using the direct matching reconstruction, which was due to the noise enhancement and aliasing artifacts in maps using the 5HB/150 ms

sequence, resulting in the wide limits of agreement in the Bland-Altman plots in **Figure 11**. Similar discrepancies were seen with SLLR-MRF to a lesser extent. Due to the improved quality of the maps, DIP-MRF yielded the closest agreement in T_1 and T_2 measured by the 15HB/254 ms and 5HB/150 ms sequences. DIP-MRF also yielded better precision *in vivo* compared to direct matching and SLLR-MRF. For T_1 , the intrasubject variability in healthy subjects was similar among MOLLI, 15HB/254 ms DIP-MRF, and 5HB/150 ms DIP-MRF. For T_2 , the intrasubject variability was lowest for 15HB/254 ms DIP-MRF, and similar between T_2 -prep bSSFP and 5HB/150 ms DIP-MRF. DIP-MRF also resulted in a lower intersubject variability for T_1 and T_2 compared to direct matching and SLLR-MRF.

Higher native T_1 and lower native T_2 were observed using MRF compared to conventional mapping sequences, which has been reported previously (50). MOLLI is known to underestimate T_1 (51), and T_2 -prep bSSFP has been reported to overestimate T_2 (52), which was observed in this study in the phantom experiment (**Figure 6** and **Supplementary Figures 5–7**). The signal model in cardiac MRF accounts for slice profile imperfections and inversion pulse efficiency, which was shown to improve accuracy and lead to higher T_1 measurements (50). Lower T_2 values have been reported with FISP-based MRF sequences compared to standard techniques in other applications, which may be related to magnetization transfer (53), intravoxel dephasing (54), and motion sensitivity along the direction of the unbalanced gradient moment (i.e., slice direction).

Increased regional variability for T_1 and to a lesser degree T_2 was observed with MRF, with higher relaxation times in the septum and lower values in the inferolateral segment. Possible explanations may include susceptibility effects (especially in

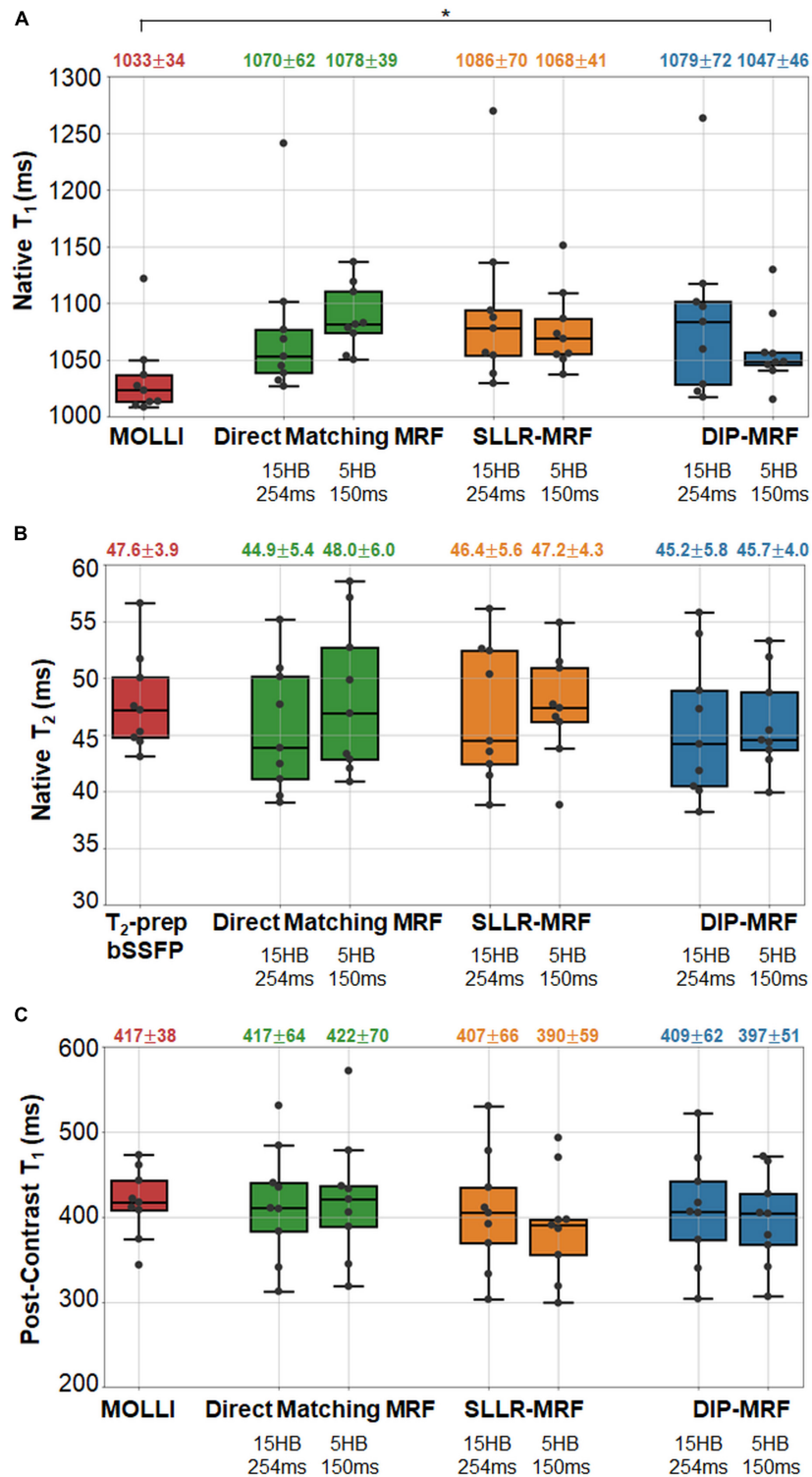


FIGURE 15 | Relaxation times in the myocardial septum in cardiomyopathy patients. The boxplots summarize the **(A)** native T_1 , **(B)** native T_2 , and **(C)** post-contrast T_1 using conventional mapping sequences, as well as 15HB/254 ms MRF and 5HB/150 ms MRF with direct matching, SLLR-MRF, and DIP-MRF reconstructions. The top of each box indicates the upper quartile, the bottom indicates the lower quartile, and the horizontal line through the middle shows the median. The numbers above each plot indicate the mean \pm standard deviation over all patients. Asterisks indicate a significant difference ($p < 0.05$) using a within-subjects ANOVA test with a Bonferroni *post-hoc* test for multiple comparisons. Native mapping was performed in all ten patients. Post-contrast MRF was acquired in all ten patients, while post-contrast MOLLI was only collected in nine patients.

the inferolateral segment); partial volume artifacts between myocardium and epicardial fat, which could be improved with water-fat separation techniques like Dixon cardiac MRF (55) or MRF with rosette k-space sampling (56); and B_1^+ inhomogeneities, which could be addressed using B_1^+ correction (57, 58). Blood relaxation times were reported for completeness; however, blood flow into and out of the 2D imaging plane is not accounted for in the MRF signal simulation and likely affects the blood T_1 and T_2 estimates. Interestingly, higher T_1 was measured in the LV compared to the RV with both MOLLI and cardiac MRF. Higher T_2 was measured in the LV with T_2 -prep bSSFP, which has been reported previously (59), but slightly lower T_2 was measured in the LV with cardiac MRF.

In summary, a DIP-MRF reconstruction that combines low-rank subspace modeling with a deep image prior was shown to reduce noise and aliasing artifacts in cardiac MRF T_1 , T_2 , and M_0 mapping, which does not require pre-training with *in vivo* data. This method enables a shortened breathhold duration and cardiac acquisition window in cardiac MRF, which has the potential to improve scan efficiency and reduce motion artifacts. Future work will explore extensions of DIP-MRF to motion-resolved (cine) MRF (60, 61) and 3D cardiac MRF (62).

DATA AVAILABILITY STATEMENT

The raw data supporting the conclusions of this article will be made available by the authors, without undue reservation.

REFERENCES

- Goldfarb JW, Arnold S, Han J. Recent myocardial infarction: assessment with unenhanced T1-weighted MR imaging. *Radiology*. (2007) 245:245–50. doi: 10.1148/radiol.2451061590
- Okur A, Kantarcı M, Kızrak Y, Yıdız S, Pirimoğlu B, Karaca L, et al. Quantitative evaluation of ischemic myocardial scar tissue by unenhanced T1 mapping using 3.0 Tesla MR scanner. *Diagn Interv Radiol*. (2014) 20:407–13. doi: 10.5152/dir.2014.13520
- Dall'Armellina E, Piechnik SK, Ferreira VM, Si QL, Robson MD, Francis JM, et al. Cardiovascular magnetic resonance by non contrast T1-mapping allows assessment of severity of injury in acute myocardial infarction. *J Cardiovasc Magn Reson*. (2012) 14:15. doi: 10.1186/1532-429X-14-15
- Park CH, Choi E-Y, Kwon HM, Hong BK, Lee BK, Yoon YW, et al. Quantitative T2 mapping for detecting myocardial edema after reperfusion of myocardial infarction: validation and comparison with T2-weighted images. *Int J Cardiovasc Imaging*. (2013) 29:65–72. doi: 10.1007/s10554-013-0256-0
- Giri S, Chung YC, Merchant A, Mihai G, Rajagopalan S, Raman SV, et al. T2 quantification for improved detection of myocardial edema. *J Cardiovasc Magn Reson*. (2009) 11:56. doi: 10.1186/1532-429X-11-56
- Baggiano A, Boldrini M, Martinez-Naharro A, Kotecha T, Petrie A, Rezk T, et al. Noncontrast magnetic resonance for the diagnosis of cardiac amyloidosis. *JACC Cardiovasc Imaging*. (2020) 13:69–80. doi: 10.1016/j.jcmg.2019.03.026
- Sado DM, White SK, Piechnik SK, Banyersad SM, Treibel T, Captur G, et al. Identification and assessment of anderson-fabry disease by cardiovascular magnetic resonance noncontrast myocardial T1 mapping. *Circ Cardiovasc Imaging*. (2013) 6:392–8. doi: 10.1161/CIRCIMAGING.112.000070
- Messroghli DR, Walters K, Plein S, Sparrow P, Friedrich MG, Ridgway JP, et al. Myocardial T1 mapping: application to patients with acute and chronic myocardial infarction. *Magn Reson Med*. (2007) 58:34–40. doi: 10.1002/mrm.21272
- Weingärtner S, Akçakaya M, Basha T, Kissinger KV, Goddu B, Berg S, et al. Combined saturation/inversion recovery sequences for improved evaluation of scar and diffuse fibrosis in patients with arrhythmia or heart rate variability. *Magn Reson Med*. (2014) 71:1024–34. doi: 10.1002/mrm.24761
- Kvernby S, Warntjes MJ, Haraldsson H, Carlhall CJ, Engvall J, Ebbens T. Simultaneous three-dimensional myocardial T1 and T2 mapping in one breath hold with 3D-QALAS. *J Cardiovasc Magn Reson*. (2014) 16:102. doi: 10.1186/s12968-014-0102-0
- Akçakaya M, Weingärtner S, Basha TA, Roujol S, Bellm S, Nezafat R. Joint myocardial T1 and T2 mapping using a combination of saturation recovery and T2-preparation. *Magn Reson Med*. (2016) 76:888–96. doi: 10.1002/mrm.25975
- Christodoulou AG, Shaw JL, Nguyen C, Yang Q, Xie Y, Wang N, et al. Magnetic resonance multitasking for motion-resolved quantitative cardiovascular imaging. *Nat Biomed Eng*. (2018) 2:215–26. doi: 10.1038/s41551-018-0217-y
- Ma D, Gulani V, Seiberlich N, Liu K, Sunshine JL, Duerk JL, et al. Magnetic resonance fingerprinting. *Nature*. (2013) 495:187–92. doi: 10.1038/nature11971
- Hamilton JI, Jiang Y, Chen Y, Ma D, Lo WC, Griswold M, et al. MR fingerprinting for rapid quantification of myocardial T1, T2, and proton spin density. *Magn Reson Med*. (2017) 77:1446–58. doi: 10.1002/mrm.26216
- Hamilton JI, Pahwa S, Adedigba J, Frankel S, O'Connor G, Thomas R, et al. Simultaneous mapping of T1 and T2 using cardiac magnetic resonance fingerprinting in a cohort of healthy subjects at 1.5T. *J Magn Reson Imaging*. (2020) 52:1044–52. doi: 10.1002/jmri.27155
- Cavallo AU, Liu Y, Patterson A, Al-Kindi S, Hamilton J, Gilkeson R, et al. CMR fingerprinting for myocardial T1, T2, and ECV quantification in patients with nonischemic cardiomyopathy. *JACC Cardiovasc Imaging*. (2019) 12:1584–5. doi: 10.1016/j.jcmg.2019.01.034

ETHICS STATEMENT

The studies involving human participants were reviewed and approved by Institutional Review Boards of the University of Michigan Medical School (IRBMED). The patients/participants provided their written informed consent to participate in this study.

AUTHOR CONTRIBUTIONS

JH: study conception and design, deep learning reconstruction implementation, data collection and analysis, manuscript preparation, and approved the submitted version.

FUNDING

This work was supported by the Michigan Institute for Clinical & Health Research (MICHR) Grant UL1TR002240, Siemens Healthineers, and NIH/NHLBI R01HL163030.

SUPPLEMENTARY MATERIAL

The Supplementary Material for this article can be found online at: <https://www.frontiersin.org/articles/10.3389/fcvm.2022.928546/full#supplementary-material>

17. Cruz G, Qi H, Jaubert O, Kuestner T, Schneider T, Botnar RM, et al. Generalized low-rank nonrigid motion-corrected reconstruction for MR fingerprinting. *Magn Reson Med.* (2022) 87:746–63. doi: 10.1002/mrm.29027
18. Pierre EY, Ma D, Chen Y, Badve C, Griswold MA. Multiscale reconstruction for MR fingerprinting. *Magn Reson Med.* (2016) 75:2481–92. doi: 10.1002/mrm.25776
19. Cline CC, Chen X, Mailhe B, Wang Q, Pfeuffer J, Nittka M, et al. AIR-MRF: accelerated iterative reconstruction for magnetic resonance fingerprinting. *Magn Reson Imaging.* (2017) 41:29–40. doi: 10.1016/j.mri.2017.07.007
20. Doneva M, Amthor T, Koken P, Sommer K, Börnert P. Matrix completion-based reconstruction for undersampled magnetic resonance fingerprinting data. *Magn Reson Imaging.* (2017) 41:41–52. doi: 10.1016/j.mri.2017.02.007
21. Zhao B, Setsompop K, Adalsteinsson E, Gagoski B, Ye H, Ma D, et al. Improved magnetic resonance fingerprinting reconstruction with low-rank and subspace modeling. *Magn Reson Med.* (2018) 79:933–42. doi: 10.1002/mrm.26701
22. Assländer J, Cloos MA, Knoll F, Sodickson DK, Hennig J, Lattanzi R. Low rank alternating direction method of multipliers reconstruction for MR fingerprinting. *Magn Reson Med.* (2018) 79:83–96. doi: 10.1002/mrm.26639
23. Cohen O, Zhu B, Rosen MS. MR fingerprinting deep reconstruction network (DRONE). *Magn Reson Med.* (2018) 80:885–94. doi: 10.1002/mrm.27198
24. Hamilton JI, Currey D, Rajagopalan S, Seiberlich N. Deep learning reconstruction for cardiac magnetic resonance fingerprinting T1 and T2 mapping. *Magn Reson Med.* (2021) 85:2127–35. doi: 10.1002/mrm.28568
25. Fang Z, Chen Y, Liu M, Lei X, Zhang Q, Wang Q, et al. Deep learning for fast and spatially-constrained tissue quantification from highly-accelerated data in magnetic resonance fingerprinting. *IEEE Trans Med Imaging.* (2019) 38:2364–74. doi: 10.1109/TMI.2019.2899328
26. Fang Z, Chen Y, Hung S, Zhang X, Lin W, Shen D. Submillimeter MR fingerprinting using deep learning-based tissue quantification. *Magn Reson Med.* (2020) 84:579–91. doi: 10.1002/mrm.28136
27. Ulyanov D, Vedaldi A, Lempitsky V. Deep image prior. *Proceedings of the IEEE Computer Society Conference on Computer Vision and Pattern Recognition.* Washington, DC: IEEE Computer Society (2018). p. 9446–54.
28. Ronneberger O, Fischer P, Brox T. U-Net: convolutional networks for biomedical image segmentation. In: Navab N, Hornegger J, Wells WM, Frangi AF editors. *Medical Image Computing and Computer-Assisted Intervention.* Berlin: Springer International Publishing (2015). p. 234–41.
29. Chakrabarty P, Maji S. The spectral bias of the deep image prior. *arXiv.* [Preprint]. (2019). Available online at: <https://doi.org/10.48550/arXiv.1912.08905> (accessed March 1, 2022).
30. Bagger DO, Leuschner J, Schmidt M. Computed tomography reconstruction using deep image prior and learned reconstruction methods. *Inverse Probl.* (2020) 36:094004.
31. Gong K, Catana C, Qi J, Li Q. PET image reconstruction using deep image prior. *IEEE Trans Med Imaging.* (2019) 38:1655–65. doi: 10.1109/TMI.2018.2888491
32. Lin YC, Huang HM. Denoising of multi b-value diffusion-weighted MR images using deep image prior. *Phys Med Biol.* (2020) 65:105003. doi: 10.1088/1361-6560/ab8105
33. McGivney DF, Pierre E, Ma D, Jiang Y, Saybasili H, Gulani V, et al. SVD compression for magnetic resonance fingerprinting in the time domain. *IEEE Trans Med Imaging.* (2014) 33:2311–22. doi: 10.1109/TMI.2014.2337321
34. Lima da Cruz G, Bustin A, Jaubert O, Schneider T, Botnar RM, Prieto C. Sparsity and locally low rank regularization for MR fingerprinting. *Magn Reson Med.* (2019) 81:3530–43. doi: 10.1002/mrm.27665
35. Hamilton JI, Jiang Y, Ma D, Chen Y, Lo WC, Griswold M, et al. Simultaneous multislice cardiac magnetic resonance fingerprinting using low rank reconstruction. *NMR Biomed.* (2019) 32:e4041. doi: 10.1002/nbm.4041
36. Hamilton JI, Seiberlich N. Machine learning for rapid magnetic resonance fingerprinting tissue property quantification. *Proc IEEE Inst Electr Electron Eng.* (2020) 108:69–85. doi: 10.1109/JPROC.2019.2936998
37. Seiberlich N, Breuer FA, Blaimer M, Barkauskas K, Jakob PM, Griswold MA. Non-Cartesian data reconstruction using GRAPPA operator gridding (GROG). *Magn Reson Med.* (2007) 58:1257–65. doi: 10.1002/mrm.21435
38. Fessler J, Sutton B. Nonuniform fast fourier transforms using min-max interpolation. *IEEE Trans Signal Process.* (2003) 51:560–74.
39. Walsh D, Gmitro A, Marcellin M. Adaptive reconstruction of phased array MR imagery. *Magn Reson Med.* (2000) 43:682–90. doi: 10.1002/(sici)1522-2594(200005)43:5<682::aid-mrm10>>3.0.co;2-g
40. Jiang Y, Ma D, Seiberlich N, Gulani V, Griswold MA. MR fingerprinting using fast imaging with steady state precession (FISP) with spiral readout. *Magn Reson Med.* (2015) 74:1621–31. doi: 10.1002/mrm.25559
41. Hargreaves B. *Variable-Density Spiral Design Functions.* (2005). Available online at: <http://mrsrl.stanford.edu/~brian/vdspiral/> (accessed June 1, 2017).
42. Winkelmann S, Schaeffter T, Koehler T, Eggers H, Doessel O. An optimal radial profile order based on the golden ratio for time-resolved MRI. *IEEE Trans Med Imaging.* (2007) 26:68–76. doi: 10.1109/TMI.2006.885337
43. Srivastava N, Hinton G, Krizhevsky A, Sutskever I, Salakhutdinov R. Dropout: a simple way to prevent neural networks from overfitting. *J Mach Learn Res.* (2014) 15:1929–58.
44. Keenan KE, Stupic KF, Boss M, Russek SE, Chenevert TL, Prasad PV, et al. Comparison of T1 measurement using ISMRM/NIST system phantom. *Proceedings of the 24th Annual Meeting of ISMRM.* Concord, CA: International Society for Magnetic Resonance in Medicine (2016). p. 3290.
45. Siemens Medical Solutions [SMS]. *MyoMaps.* (2018). Available online at: <https://usa.healthcare.siemens.com/magnetic-resonance-imaging/options-and-upgrades/clinical-applications/myomaps> (accessed February 27, 2018).
46. Messroghli DR, Radjenovic A, Kozerke S, Higgins DM, Sivananthan MU, Ridgway JP. Modified Look-Locker inversion recovery (MOLLI) for high-resolution T1 mapping of the heart. *Magn Reson Med.* (2004) 52:141–6. doi: 10.1002/mrm.20110
47. Bland JM, Altman DG. Statistical methods for assessing agreement between two methods of clinical measurement. *Lancet.* (1986) 1:307–10.
48. Cerqueira MD. Standardized myocardial segmentation and nomenclature for tomographic imaging of the heart: a statement for healthcare professionals from the cardiac imaging committee of the council on clinical cardiology of the American heart association. *Circulation.* (2002) 105:539–42. doi: 10.1161/hc0402.102975
49. Barbano R, Leuschner J, Schmidt M, Denker A, Hauptmann A, Maaß P, et al. Is deep image prior in need of a good education? *arXiv.* [Preprint]. (2021). Available online at: <https://doi.org/10.48550/arXiv.2111.11926> (accessed March 1, 2022).
50. Hamilton JI, Jiang Y, Ma D, Lo W-C, Gulani V, Griswold M, et al. Investigating and reducing the effects of confounding factors for robust T1 and T2 mapping with cardiac MR fingerprinting. *Magn Reson Imaging.* (2018) 53:40–51. doi: 10.1016/j.mri.2018.06.018
51. Kellman P, Hansen MS. T1-mapping in the heart: accuracy and precision. *J Cardiovasc Magn Reson.* (2014) 16:2. doi: 10.1186/1532-429X-16-2
52. Baeßler B, Schaarschmidt F, Stehning C, Schnackenburg B, Maintz D, Bunck AC. Cardiac T2-mapping using a fast gradient echo spin echo sequence - first in vitro and in vivo experience. *J Cardiovasc Magn Reson.* (2015) 17:67. doi: 10.1186/s12968-015-0177-2
53. Gloor M, Scheffler K, Bieri O. Quantitative magnetization transfer imaging using balanced SSFP. *Magn Reson Med.* (2008) 60:691–700. doi: 10.1002/mrm.21705
54. Assländer J, Glaser SJ, Hennig J. Pseudo steady-state free precession for MR-fingerprinting. *Magn Reson Med.* (2017) 77:1151–61. doi: 10.1002/mrm.26202
55. Jaubert O, Cruz G, Bustin A, Schneider T, Lavin B, Koken P, et al. Water-fat Dixon cardiac magnetic resonance fingerprinting. *Magn Reson Med.* (2019) 83:2107–23. doi: 10.1002/mrm.28070
56. Liu Y, Hamilton J, Eck B, Griswold M, Seiberlich N. Myocardial T1 and T2 quantification and water-fat separation using cardiac MR fingerprinting with rosette trajectories at 3T and 1.5T. *Magn Reson Med.* (2020) 85:103–19. doi: 10.1002/mrm.28404
57. Ma D, Coppo S, Chen Y, McGivney DF, Jiang Y, Pahwa S, et al. Slice profile and B1 corrections in 2D magnetic resonance fingerprinting. *Magn Reson Med.* (2017) 78:1781–9. doi: 10.1002/mrm.26580

58. Buonincontri G, Schulte RF, Cosottini M, Tosetti M. Spiral MR fingerprinting at 7T with simultaneous B1 estimation. *Magn Reson Imaging.* (2017) 41:1–6. doi: 10.1016/j.mri.2017.04.003
59. Emrich T, Bordonaro V, Schoepf UJ, Petrescu A, Young G, Halfmann M, et al. Right/left ventricular blood pool T2 ratio as an innovative cardiac MRI screening tool for the identification of left-to-right shunts in patients with right ventricular disease. *J Magn Reson Imaging.* (2022) 55:1452–8. doi: 10.1002/jmri.27881
60. Hamilton JI, Jiang Y, Eck B, Griswold M, Seiberlich N. Cardiac cine magnetic resonance fingerprinting for combined ejection fraction, T1 and T2 quantification. *NMR Biomed.* (2020) 33:e4323. doi: 10.1002/nbm.4323
61. Jaubert O, Cruz G, Bustin A, Schneider T, Koken P, Doneva M, et al. Free-running cardiac magnetic resonance fingerprinting: joint T1/T2 map and cine imaging. *Magn Reson Imaging.* (2020) 68:173–82. doi: 10.1016/j.mri.2020.02.005
62. Cruz G, Jaubert O, Qi H, Bustin A, Milotta G, Schneider T, et al. 3D free-breathing cardiac magnetic resonance fingerprinting. *NMR Biomed.* (2020) 33:e4370. doi: 10.1002/nbm.4370

Conflict of Interest: This study received funding from Siemens Healthineers (Erlangen, Germany). The funder had no involvement with any aspect of the study design, data collection, interpretation of results, or manuscript preparation.

The author declares that the research was conducted in the absence of any commercial or financial relationships that could be construed as a potential conflict of interest.

Publisher's Note: All claims expressed in this article are solely those of the authors and do not necessarily represent those of their affiliated organizations, or those of the publisher, the editors and the reviewers. Any product that may be evaluated in this article, or claim that may be made by its manufacturer, is not guaranteed or endorsed by the publisher.

Copyright © 2022 Hamilton. This is an open-access article distributed under the terms of the Creative Commons Attribution License (CC BY). The use, distribution or reproduction in other forums is permitted, provided the original author(s) and the copyright owner(s) are credited and that the original publication in this journal is cited, in accordance with accepted academic practice. No use, distribution or reproduction is permitted which does not comply with these terms.